

AD-A089 811

CAMBRIDGE UNIV (ENGLAND) CAVENDISH LAB

F/6 20/4

REDUCTION OF AERODYNAMIC DRAG.(U)

MAY 80 J CLARK, J E FIELD, W A WILBY

AFOSR-79-0057

UNCLASSIFIED

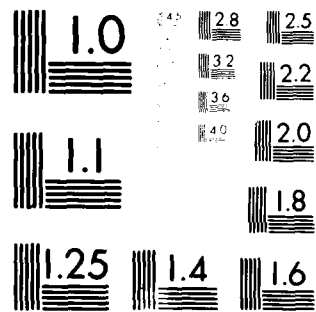
AFOSR-TR-80-0748

NL

1 OF 2

ALL
Pages





MICROCOPY RESOLUTION TEST CHART
NATIONAL BUREAU OF STANDARDS-1963-A

UNIVERSITY OF CAMBRIDGE
DEPARTMENT OF PHYSICS

4

AD A089811

REDUCTION OF AERODYNAMIC DRAG

DR J. CLARK } PRINCIPAL INVESTIGATORS
DR J.E. FIELD }
W.A. WILEY RESEARCH STUDENT

LEVEL

CAVENDISH LABORATORY
UNIVERSITY OF CAMBRIDGE
MAY 1980

*Cambridge Univ.
Cavendish
Lab*

INTERIM SCIENTIFIC REPORT No. 1
1 April 1979 - 31 March 1980

DTIC
ELECTE
SEP 24 1980
C

Approved for public release;
distribution unlimited

Prepared for:

U.S. Air Force Office of Scientific Research (AFOSR)

and

European Office of Aerospace Research and Development,
London, England

Approved for public release;
distribution unlimited.

Cavendish Laboratory, Madingley Road, Cambridge CB3 0HE.

80 9 25 068

DDC FILE COPY

UNCLASSIFIED

REPORT DOCUMENTATION PAGE		READ INSTRUCTIONS BEFORE COMPLETING FORM
1. REPORT NUMBER (18) AFOSR-TR-80-0748	2. GOVT ACCESSION NO. AD-A089847	3. RECIPIENT'S CATALOG NUMBER
4. TITLE (and Subtitle) REDUCTION OF AERODYNAMIC DRAG		5. TYPE OF REPORT & PERIOD COVERED INTERIM
7. AUTHOR(s) CLARK FIELD WILBY		6. PERFORMING ORG. REPORT NUMBER
8. CONTRACT OR GRANT NUMBER(s) AFOSR-79-0057		9. PERFORMING ORGANIZATION NAME AND ADDRESS CAVENDISH LABORATORY UNIVERSITY OF CAMBRIDGE CAMBRIDGE CB3 0HE, ENGLAND
10. PROGRAM ELEMENT, PROJECT, TASK AREA & WORK UNIT NUMBERS (16) 2307/A2 61102F (17) A2		11. CONTROLLING OFFICE NAME AND ADDRESS AIR FORCE OFFICE OF SCIENTIFIC RESEARCH/NA BUILDING 410 BOLLING AFB, DC 20332
12. REPORT DATE (11) May 80		13. NUMBER OF PAGES 118
14. MONITORING AGENCY NAME & ADDRESS (if different from Controlling Office) Interim scientific rept. no. 1. 1 Apr 79-31 Mar 80		15. SECURITY CLASS. (of this report) UNCLASSIFIED
15a. DECLASSIFICATION/DOWNGRADING SCHEDULE		
16. DISTRIBUTION STATEMENT (of this Report) Approved for public release; distribution unlimited.		
17. DISTRIBUTION STATEMENT (of the abstract entered in Block 20, if different from Report)		
18. SUPPLEMENTARY NOTES		
19. KEY WORDS (Continue on reverse side if necessary and identify by block number) AERODYNAMICS MOLECULAR AERODYNAMICS DRAG REDUCTION RADIOACTIVITY BOUNDARY LAYERS TURBULENCE		
20. ABSTRACT (Continue on reverse side if necessary and identify by block number) This report describes the construction of a miniature aerodynamic skin friction drag balance and its use in a preliminary investigation of the drag reducing effect of boundary layer irradiation. The balance is of the null-position type and is operated using an automatic control system to maintain the null-position of the drag plate. High accuracy and stability are observed at flow velocities up to 0.8 Mach Number, and a resolution of less than 0.5% of changes in drag force can be achieved. In preliminary experiments irradiation of the boundary		

UNCLASSIFIED

UNCLASSIFIED

layer with B particles from a 120 mCi ^{147}Pm source has given drag reductions of $5 \pm 3\%$ at flow velocities up to 0.6 Mach Number. In future work more accurate data on the drag reduction will be obtained and the physical basis of the phenomenon studied.

approx. $5 + \text{ or } - 3\%$

UNCLASSIFIED

GRANT NO: AFOSR-79-0057

4

REDUCTION OF AERODYNAMIC DRAG

Dr J. Clark)
Principal Investigators
Dr J. E. Field)
W. A. Wilby Research Student

Cavendish Laboratory
University of Cambridge
Cambridge, U. K.

In Scientific Report No. 1

1 April 1979 - 31 March 1980

Approved for public release;
distribution unlimited.

Prepared for:

U. S. Air Force Office of Scientific Research (AFOSR).

and

European Office of Aerospace Research and Development,
London, England.

3

AIR FORCE OFFICE OF SCIENTIFIC RESEARCH (AFSC)
NOTICE OF TRANSMITTAL TO DDC
This technical report has been reviewed and is
approved for public release IAW AFR 190-12 (7b).
Distribution is unlimited.
A. D. BLOSE
Technical Information Officer

2

INDEX

	Page
List of Symbols	(ii)
Table of Constants	(iii)
List of Tables	(iv)
List of Figures	(v)
Preface	1
1 Introduction	2
2 Description of Drag Balance System	6
2.1 Windtunnel	7
2.2 Prototype Skin Friction Drag Balance	8
2.3 Automatic Control System	11
2.4 Skin Friction Drag Balance	13
3 Experimental Work	16
3.1 Calibration and Initial Tests of Prototype Balance	17
3.2 Performance Tests of Automatic Control System	21
3.3 Drag Data Obtained with Prototype Balance and Control System	21
3.4 Calibration and Initial Tests of Drag Balance	22
3.5 Construction of Radioactive Drag Plates	30
3.6 Effect of Boundary Layer Irradiation	33
4 Summary of Results	37
5 Discussion and Conclusions	38
App. A Problems Encountered	40
App. B References	41
App. C Bibliography	42

Accession For	
NTIS GRA&I	<input checked="checked" type="checkbox"/>
DTIC TAB	<input type="checkbox"/>
Unannounced	<input type="checkbox"/>
Justification	
By _____	
Distribution/	
Availability Codes	
Dist	Avail and/or Special

List of Symbols

τ	local shear stress
D	drag force
u	flow velocity (u_{∞} free stream u_0 centre-line)
x	coordinate measured along surface
y	coordinate measured normal to surface
ρ	density
μ	viscosity
$\nu = \mu/\rho$	kinematic viscosity
$c_f = \frac{\tau}{\frac{1}{2}\rho u_0^2}$	dimensionless drag coefficient
$Re = \frac{vx}{\nu}$	Reynolds Number (R_c based on tunnel thickness R_l based on plate length)
δ	boundary layer thickness
a	half thickness of tunnel
a_0	speed of sound
$M = u_0/a_0$	Mach Number
P_{ps}	pitot static pressure
P_s	static pressure (gauge)
P_{at}	atmospheric pressure
γ	ratio of specific heats (C_p/C_v)
I	coil current
R	strain gauge bridge reading
r	regression coefficient
l	load; plate length
W	plate width
A	plate area, amplitude ratio

Table of Constants

γ	1.401	(for air)
a_o	340.3 mS^{-1}	"
μ	$1.789 \times 10^{-5} \text{ kg m}^{-1} \text{ s}^{-1}$	"
ρ	1.225 kg m^{-3}	"
P_{AT}	760 mm Hg; 101.3 kPa	

List of Tables

	Page
1 Spring Calibration	18
2 Prototype Balance Calibration	19
3 First Balance Calibration	25
4 First Set of Drag Measurements	26
5 First Set of Drag Values	27
6 Second Balance Calibration	28
7 Second Set of Drag Measurements	28
8 Second Set of Drag Values	29
9 Specifications of Radioactive Foils	31
10 Drag Measurements with Active Plates	34
11 Mean Drag Values with Active Plates	35
12 Summary of Results	36

List of Figures

- 1 View of Windtunnel System
- 2 Side View of Windtunnel Transition Section
- 3 Schematic Diagram of Prototype Skin Friction Balance
- 4 View of Prototype Skin Friction Balance
- 5 Side View of Calibration Spring Assembly
- 6 Front View of Calibration Spring
- 7 Schematic Diagram of Calibration Procedure for Spring
- 8 Schematic Diagram of Drag Balance Automatic Control System
- 9 Schematic Diagrams of Signal Conditioner and Control Circuit
- 10 Circuit Diagram of Control Circuit
- 11 View of Windtunnel and Drag Balance System
- 12 View of Skin Friction Drag Balance
- 13 Top Inside View of Balance
- 14 View from Below of the Inside of the Drag Balance
- 15 Photograph of Levelling Plate
- 16 Photograph of Balance During Calibration
- 17 Flat Plate Approximation Applied to Windtunnel and Balance
- 18 Typical Calibration Curve for the Strain Gauge Spring
- 19 Typical Calibration Curve of Prototype Drag Balance using Strain Gauge Spring
- 20 Final Calibration of Prototype Drag Balance
- 21 Shear Stress vs Flow Velocity
- 22 Drag Coefficient vs Reynolds Number
- 23 Control Circuit Output for a Range of Trigger Conditions
- 24 Response Curves for the Drag Balance Control System
- 25 Performance Curves for the Automatic Control System
- 26 Drag Coefficient vs Reynolds Number

27	Response Curve of Drag Balance
28	Initial Test of Drag Balance
29	Coil Current vs Pitot Static Pressure
30	Typical Calibration Curve for the Drag Balance
31	Drag Coefficient vs Reynolds Number
32	Coil Current vs Pitot Static Pressure
33	Diagrams Showing Foil Mounting Procedure
34	Photograph Illustrating Precautions Taken When Handling Radioactive Sources
35	Active Drag Plate

Figs 1 - 16 are to be found after p. 15

Fig. 17 is to be found after p. 16

Figs 18 - 35 are to be found after p. 36

Preface

This report describes the construction of a miniature aerodynamic skin friction drag balance and its use in a preliminary investigation of the drag reducing effect of boundary layer irradiation.

The balance is of the null-position type and is operated using an automatic control system to maintain the null position of the drag plate. High accuracy and stability are observed at flow velocities up to 0.8 Mach Number, and a resolution of less than 0.5% of changes in drag force can be achieved.

In preliminary experiments irradiation of the boundary layer with β particles from a 120 mCi ^{147}Pm source has given drag reductions of $\sim 5 \pm 3\%$ at flow velocities up to 0.6 Mach Number.

In future work more accurate data on the drag reduction will be obtained and the physical basis of the phenomenon studied.

1 Introduction

The problem of reducing the drag of a body, such as an aircraft, moving through a fluid can be attacked either by improving the streamlining of the body, i.e. reducing the "pressure" or "form" drag (this will not be further discussed) or by altering the fluid/surface interaction in such a way as to reduce the local shear stress ("skin friction") at the surface^{1,2}.

The region of the fluid in which shear stresses become important is generally restricted to a thin layer on the surface of the body, the boundary layer, in which the fluid velocity rises from zero at the surface ("no slip" condition) to the free stream value. (For a detailed discussion of boundary layer theory see, for example, Refs. 1, 3, 4.) It follows that the properties of this boundary layer and the adjacent surface are of paramount importance in determining the drag forces acting on the body and are the focus of any investigation into skin friction drag reduction.

In this work an investigation has been made of the effect of irradiation of the boundary layer by ionising particles. The incentive for this new approach comes from work performed using a torsion disc viscometer in an investigation of the effect of ionisation on the viscosity of a number of gases^{5,6}. (Note that in these references the activity level given for the ²¹⁰Po coated disc is incorrect; the lower value of 0.5 to 1.0 mCi cm⁻² is probably nearer to the correct activity.) Some significant changes in the viscosity were observed, the most prominent being an increase of 5.2% for Ar at 1 atm and a 7.6% reduction for dry (i.e. ~ 5 vppm H₂O) air at 1 mm Hg pressure.

The present research is investigating this effect under conditions which more nearly simulate those of flight, i.e. gas static pressure close

to 1 atmosphere and flow velocities up to ~ 0.8 Mach Number with both moist and dry air in addition to other gases.

To investigate methods of drag reduction, one must be able to measure skin friction drag accurately. There are several possible approaches to this notoriously difficult problem and we briefly review the most important. (For a more detailed discussion and an account of a direct measurement of skin friction see Ref. 7.)

For flow satisfying the "no slip" condition, the skin friction shear stress is given by

$$\tau = \left(\mu \frac{\partial u}{\partial y} \right)_{y=0}$$

This expression is valid for both laminar and (due to the presence of the sub-boundary layer) turbulent flows. It follows that a determination of viscosity and of the velocity profile in the boundary layer will yield a value for the skin friction. However, it is difficult (particularly if the boundary layer is thin) to accurately determine the velocity profile and errors in $\partial u / \partial y$ may be appreciable. (It should be noted that most instruments commonly used for velocity measurements, for example, the pitot tube and the hot-wire anemometer, are, due to their size, of limited use close to the surface.)

Heat transfer measurements can also (by virtue of the Reynolds analogy between heat and momentum transfer) be used to measure shear stress^{1,7}, as with hot-film shear gauges for example. These have the drawback of requiring extensive calibration and would not, in any case, be appropriate to an investigation in which the shear stresses on different types of surface were required.

This brings us to the most straightforward method (in principle)

of skin friction measurement, that of a direct measurement of the shear stress acting on a small moveable element (drag plate) of the aerodynamic surface; the drag force being determined by the application of a measured opposing force to the moveable element. The system must be extremely sensitive (typical shear stresses for laminar subsonic flow might range from $0.01 - 1.0 \text{ gf cm}^{-2}$) and this can make it difficult to achieve high accuracy.

An important consideration with this method of measurement is the gap around the moveable element; if it results in a flow perturbation, as would be the case when a pressure difference exists between opposite sides of the element, inaccurate results will be obtained. The alignment of the drag plate will obviously be an extremely critical factor; the face of the plate must be accurately flush with the surface. A misalignment of as little as $10 \text{ }\mu\text{m}$ could change drag measurements by several percent. For a detailed quantitative discussion of these types of error sources see Ref. 8. With regard to the way in which the force is balanced, it is possible either to measure the deflection of the plate against some resilient system (spring flexures or torsion wires for example) or to maintain the plate at a null position by the application of a measured force (e.g. magnets and coils). The null position method has the advantage that the gap geometry is unaltered and that slow changes in the elastic properties of supporting and resilient members are not important.

Other factors which must be considered are the effects of temperature, external vibration and flow fluctuations on the calibration and response of the balance system. The best system for this work seems to be a null position drag balance mounted in the test section of a miniature windtunnel designed to give accurately reproducible flows, and this approach has, in fact, been used. For simplicity, the moving element

or drag plate forms part of the wall of the windtunnel used. A more detailed description of the balance and tunnel is given in Section 2.

2 Description of Drag Balance System

The drag balance system consists of a miniature blow-down windtunnel with a sensitive skin friction balance of the null position type mounted in the test section. The moveable drag element forms part of the windtunnel wall. The small size of the tunnel makes it easy to construct and permits the use of different working gases with compressed gas cylinders as the supply.

The emphasis has been on developing a balance which can reliably detect small changes in the surface shear stress on different types of drag element over a wide range of flow velocities, rather than on an absolute determination of the skin friction coefficient. This enables the balance and windtunnel to be of a particularly simple form as, provided the flow can be accurately reproduced, a detailed knowledge of boundary layer shape, side wall effects, pressure gradient effects* and so on is not essential.

With the present system, the resolution of a change in drag of as little as $\frac{1}{2}\%$ is thought to be possible.

By making some approximations, it is possible to derive a theoretical relationship between the measured drag and the Reynolds Number of the flow; in the range of validity of the approximations good agreement is reached with the drag data obtained in this work.

* i.e. pressure gradient effects as they relate to the airflow pattern. A possible source of error with this design is the pressure difference acting on the ends of the drag plate. Given the small pressure gradient along the plate, the small pressure difference between the flow and the housing, and the gap size, relatively large in this context, it was felt that no significant pressure difference would be maintained over an appreciable area of the plates ends. In the near future, the magnitude of this effect will be measured directly.

2.1 Windtunnel

The miniature windtunnel used in this work is intended to give two-dimensional isentropic laminar flow at the test section with low levels of turbulence and a static pressure near to atmospheric for flow velocities of up to 0.8 Mach Number.

For simplicity, the tunnel is of the "blow-down" type and runs with either air from a compressor which provides up to 68 cu. ft./min. ($2.5 \text{ m}^3/\text{min}$) at approx. 100 psi (700 kPa), or from compressed gas cylinders containing pure gases or dry (zero grade) air at 2000 psi (1.4 MPa) and having a volume at s.t.p. of 6.38 m^3 .

The essential features of the system are shown in fig. 1. The pressurised gas is fed via appropriate pressure regulators (usually two in series to reduce the effect of inlet pressure changes on flow rate) into the turbulence suppressor tank (maximum pressure ~ 10 psi or 70 kPa). This cylindrical copper tank contains a "honeycomb" array of over 1,400 thin walled glass tubes of approximately 0.46 m in length and also two screens of 100 mesh stainless steel cloth at the outlet end. This combination should remove any large scale turbulence from the airflow. A fairing inside the tank then guides the air into the rectangular stagnation section.

The cross-sectional area of the flow is then reduced further to that of the balance section in a two stage transition, the final cross-section being largely determined by the volume flow rate obtainable from the gas source and the desire for two dimensional flow over as wide a section of the wall as possible.

The wall shape in each transition stage is two circular arcs of opposite curvature (see fig. 2). This shape is easy to machine and

gives a smooth reduction in channel width.

The reduction from 51 mm x 126 mm at the stagnation section to approximately 5.0 mm x 20.0 mm for the first balance and approximately 5.0 mm x 30.6 mm for the second balance is achieved over a distance of about 0.3 m. (The increase in width of the second section reduces the maximum speed somewhat, but decreases the importance of side wall boundary layers at lower speeds.) This section of the tunnel is constructed from polymethylmethacrylate (PMMA).

After the balance section comes a flexible stainless steel duct of 0.15 m diameter which exhausts to the outside of the building. This permits the use of asphyxiating or explosive gases, and prevents any hazard arising in the unlikely event of leakage from the radioactive sources used in the experiments. (It should be noted that all work, even with air and no radioactive sources, is conducted with the duct in place, as its presence alters the flow parameters sufficiently for there to be apparent change in measured drag of the same order as the resolution of the system.)

2.2 Prototype Skin Friction Drag Balance

A schematic diagram of the prototype null position drag balance is given in fig. 3, and a photograph in fig. 4.

The moveable element is a steel plate of dimensions 73.0 mm x 19.1 mm x 6.9 mm fixed to a supporting steel plate (drilled for lightness) and suspended by flat steel springs attached to a framework of Invar Steel. Damping of the plate is provided by small glass dashpots containing an oil of high viscosity (normally used for vacuum work)

acting on an aluminium vane attached to the drag plate support.

The clearance between the plate and the PMMA wall of the tunnel is approximately 0.50 mm front and back and 0.25 mm at the sides. The plate is levelled by removing the balance and top section of the tunnel as one piece and then adjusting three screws on the supporting structure, alignment being checked with dial gauges. The balance housing is made of PMMA and is sealed onto the base by a rubber gasket which ensures airtightness.

Position indication for the plate is provided by a Schaevitz Linear Variable Differential Transformer (LVDT) having a range of $\pm 0.010"$ (± 0.25 mm); readout is obtained from a Schaevitz CAS-025 Signal Conditioner connected to a voltmeter. The output is roughly calibrated at 15 mV/ μ m displacement by displacing the plate a known distance using feeler gauges. The null position, 0 V output from the transformer, is maintained to within ~ 5 -10 μ m (depending on flow velocity) by adjusting the current in a solenoid coil (800 turns of 38 SWG polyurethane coated copper wire, 23 Ω resistance) acting on a $\frac{1}{4}"$ (6.35 mm) AlNiCo-6 permanent magnet attached to the drag plate. The coil current is limited to 200 mA (giving a coil surface temperature of 55°C) corresponding to ~ 15 gf drag. Thermocouples are used to monitor coil and housing temperatures.

The average flow velocity at the balance is determined from the pressure at the stagnation section by the usual expression for an isentropic contraction

$$\left(\frac{P + P_{AT}}{P_{AT}} \right) = \left(1 + \frac{(\gamma - 1)}{2} M^2 \right)^{\gamma/(\gamma - 1)}$$

where P is the gauge stagnation pressure and the static pressure at the

balance is assumed to be atmospheric. The stagnation pressure is read on a precision manometer and can typically be determined to an accuracy of $\sim 0.2\%$. Calibration of the balance is performed using a thin (0.004" or 0.1 mm) flat, constant strength cantilever spring with four strain gauges cemented to it, giving a resistance bridge with four active arms. The gauges are M-line MA-06-125AC-350 (steel compensated) and readout is from a Phillips PR9307 Carrier Wave Measuring Bridge. The spring is itself calibrated by being clamped horizontally and different known weights (analytical balance weights) hung from it. The calibration of the balance is then achieved by moving the spring (attached to the drag plate by a nylon thread) along a microscope type slide (see figs 5, 6, 7). This approach was adopted in preference to the more obvious methods in the hope that the absence of sliding or rolling friction in the calibration system might lead to a superior calibration. However, although adequate calibrations could be obtained, the non-linearity of the calibrations, the double calibration procedure and the drift of the spring calibration turn out to outweigh the potential advantages and this method was not subsequently used.

Other problems experienced with the prototype balance are difficulty of control (to hold a particular flow velocity and accurately adjust the current in the coil at the same time is a difficult two man job); the levelling procedure is not sufficiently accurate; adjusting the plate to hang squarely in the gap in the tunnel wall and without any friction between coil and magnet or LVDT and core is an extremely difficult procedure; some magnetic sticking also occurred probably due to slight magnetisation of the drag plate or steel base of the balance. These latter factors make it hard to get an adequate degree of reproducibility of results on changing drag plates. The former problem has been overcome by the development of an automatic control system (see Section 2.3).

Data taken with the prototype balance indicates that the basic design is satisfactory and an improved model has been constructed which does not have the drawbacks mentioned above. This is described in Section 2.4.

2.3 Automatic Control System

As mentioned in Section 2.2, it is difficult to control the prototype balance by hand; the regulator requires constant fine adjustment to cope with inlet pressure changes and to control the coil current at the same time to an acceptable degree of accuracy requires two people. Accordingly a control circuit was designed which would interface between the LVDT signal conditioner and the coil power supply and act in such a way as to maintain the null position of the plate, i.e. 0V output from the LVDT (see fig. 8). The power supply has a high impedance input socket accepting voltages of ~ -1 V to $+1$ V, giving proportional output currents from a power transistor of ~ -250 mA to $+250$ mA with a $20\ \Omega$ load. The control circuit must therefore increase its output voltage if the LVDT voltage is positive, decrease its output voltage if the LVDT voltage is negative, and hold its output if the LVDT voltage is zero (or close to zero).^{*} The circuit must also be stable with regard to external excitation (flow fluctuations, floor vibrations).

It can be seen that a direct feedback system is not appropriate and would make the system unstable. An integrating system would, in

* A downstream displacement gives a +ve output requiring a +ve current to balance it; the null position is set to be close to zero by sliding the LVDT in its mount; small tare or zero currents through the coil then hold it at the null position.

theory, work, but in the absence of vibration might be slow to approach zero; with vibration it is possible (depending on the phase lag and time constant of the system) that the system could be unstable.

A system was designed which would make adjustments in small stages, giving the balance time to respond to each stage before proceeding. A circuit building up/down a fine staircase voltage for positive/negative inputs was used; this has the same response speed even at voltages close to zero. After some initial design work, the circuit shown in figs 9, 10 was constructed and found to perform satisfactorily.

The LVDT output is fed (via an RC filter which removes the 2.5 kHz ripple on the LVDT output and other high frequency signals) into an amplifier stage giving a gain of up to $\sim 10^3$. The amplifier output stages are then used to trigger Schmitt Nand gates whose output gates clock pulses from a timer chip. (The circuit is symmetrical over this stage, different halves of the circuit being used to handle positive and negative signals.) The pulses are then fed via opposed diode-zener diode combinations to a capacitor bank; the diodes prevent leakage of charge when the gated clock outputs are at zero. The capacitors are of the polycarbonate type which have a very low leakage rate (see fig. 10).

The circuit therefore takes the input signal, amplifies it, and, if large enough, triggers the passage of voltage pulses of the appropriate polarity to the capacitor bank where each pulse adds or removes a step from the staircase output voltage. For an input between the trigger levels, the output voltage remains almost constant; the decay rate being negligible for output voltages in the designed working range of ± 1 V. Trigger levels can be adjusted using the 10 k Ω and 500 k Ω potentiometers (zero offset and gain adjust) in the amplifier stage to

anything from a few mV to a few volts; for use with the drag balance they are set at ± 3.5 mV (± 11 mV with the prototype). The clock chip frequency and mark/space ratio may be adjusted using the 2 M Ω potentiometers. For use with the drag balance, the frequency is set to ~ 70 Hz with a pulse width (-ve at the clock stage) of 2.7 ms and a dead time of 11.5 ms.

An evaluation of the performance of the drag balance control system is given in Section 3.2.

2.4 Drag Balance

The principle of the drag balance is the same as for the prototype. Photographs showing the windtunnel system and balance are given in figs 11-14.

The drag plate (brass, 74.4 mm x 19.35 mm x 6.85 mm) is attached to the "crossbar" on an H shaped bakelite holder supported from a rigid duralumin box by 12 wires (steel piano wire 0.010", 0.25 mm, in diameter and ~ 100 mm long); up and down at the end of each arm and side to side at the centre of each arm. This constrains the plate to motion parallel to the flow direction only. The duralumin housing has ports for access top and bottom, sealed with perspex windows and O rings, and panels at the front for electrical and pressure lead throughs. The supporting wires are raked slightly ($\sim 1^\circ$) and are fixed to tensioning screw adjusters. This permits extremely accurate levelling and location of the drag plate within the hole in the perspex wall of the windtunnel; the clearance is about 0.25 mm front and back and 0.10 mm at the sides. The wires are adjusted to have, as far as possible, similar tensions;

this can be achieved by tuning them! The tensions are such that the resonant frequency of the balance is ~ 30 Hz. Plate changing is accomplished by removing a section of the underside tunnel wall and dropping the drag plate through.

Plate alignment is by an electrical resistance method, using a levelling plate (see fig. 15) consisting of four brass contacts set in an insulating block. The block has two ridges which are held against the upper windtunnel surface and the brass contacts (accurately coplanar with the ridges) line up with the edges of the drag plate. A 9 V potential is applied between the drag plate and the contacts; electrical contact is indicated by the light emitting diodes (LED's) which can be seen in the right hand PMMA panel on the balance. The tensions in the supporting wires are adjusted until all four LED's flicker as the plate swings. This has proved to be an extremely accurate and reproducible method of aligning the drag plate.

The LVDT used has a range of ± 0.025 " (0.65 mm) and the bridge output is calibrated at ~ 20 mV/ μ m.

The drag force is balanced by two solenoidal coils of 1350 turns of 38 SWG polyurethane coated copper wire on a 12 mm o/d, 1 mm thick, aluminium former 25 mm long acting on 10 mm diameter AlNiCo-6 magnets. This allows much higher drags to be balanced, permitting investigations in the turbulent regime. The coils are connected in parallel (to give equal forces) and have resistances of 56 and 57 Ω . The coils are enclosed in aluminium housings filled with a heat sink compound and fixed to the duralumin wall of the housing which acts as a heat sink. Thermocouples are used to monitor coil temperatures; compared with the previous coil only negligible temperature rises are recorded. Adjustment of the clearance between the core and casing of the LVDT and also of the magnets and coils is achieved by pivoting them about points which are

nominally lined up; if the alignment is not sufficiently accurate clearance is obtained merely by altering the angles at which the components are clamped.

Damping is by the same method as before but with a larger vane area giving a damping ratio of about 0.14.

The ACS maintains the plate position to better than 5 μm during steady running.

The centreline flow velocity at the balance section is determined from a pitot tube and static orifice 15 mm downstream from the drag plate. (It is assumed that there is no transverse pressure gradient.) The pitot tube has a slightly smoothed flat end and has an o/d of 1.25 mm, and i/d of 0.65 mm, and a length of ~ 25 mm before the stem. The static orifice has the same diameter as the pitot tube. The static pressure at the plate and the difference between this and the housing pressure are also measured; the latter gives a sensitive check for leaks from the housing. The flow static temperature and balance housing temperature are measured using thermocouples. Calibration of the balance is performed by hanging weights from a thread attached to the damping vane and passing through the balance housing wall and over a pulley (see fig. 16). The pulley is small and light and is mounted using miniature precision bearings. The weights used are accurately weighed (0.6970 ± 0.0003 gf each) steel spheres (small ball bearings) and are handled using a slightly magnetised rod to prevent contamination. The use of bearings rather than analytical balance weights minimises the disturbance to the drag balance during loading (up to ~ 15 gf). Extremely accurate calibrations can be made by this method, and with the new levelling and plate changing techniques a high degree of reproducibility between data for similar drag plates can be attained.

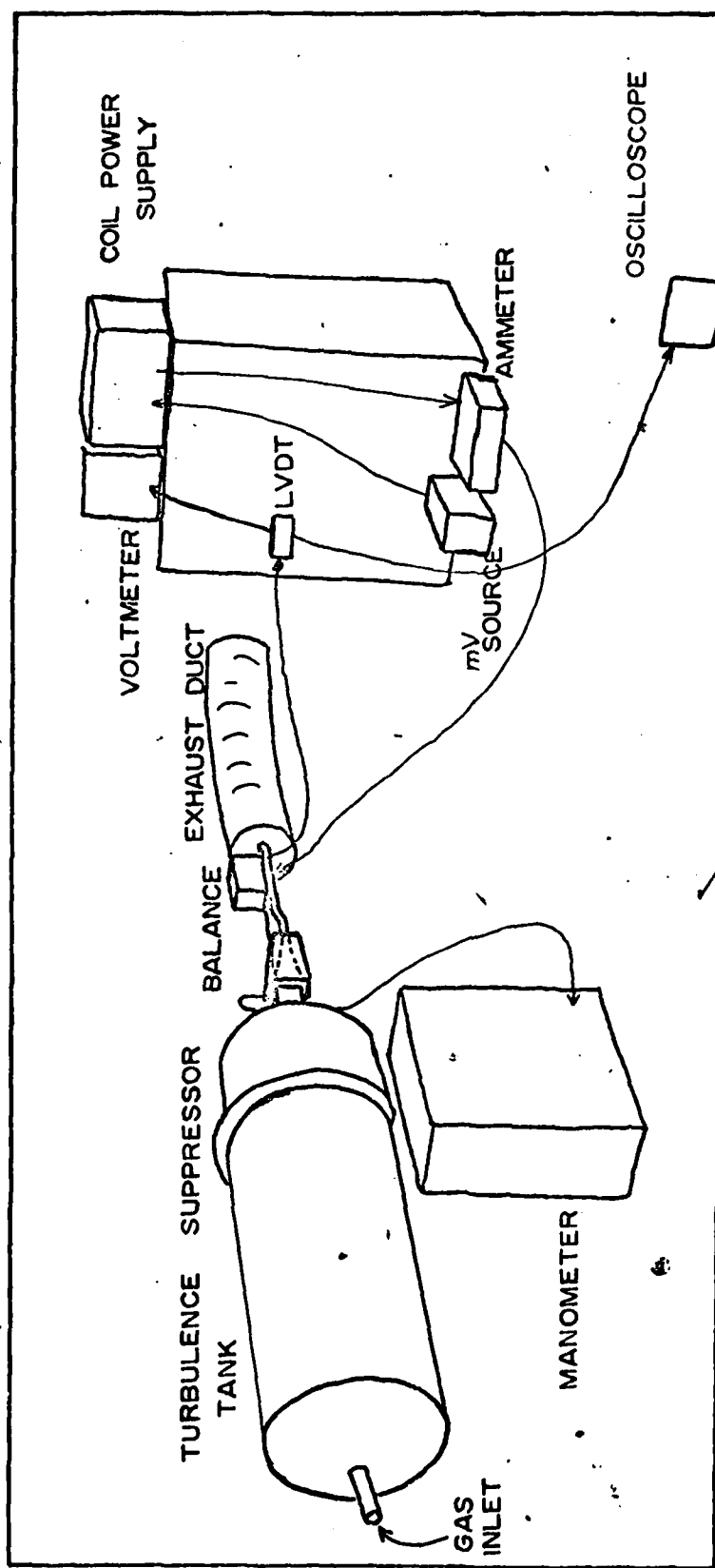


Figure 1 VIEW OF WINDTUNNEL SYSTEM

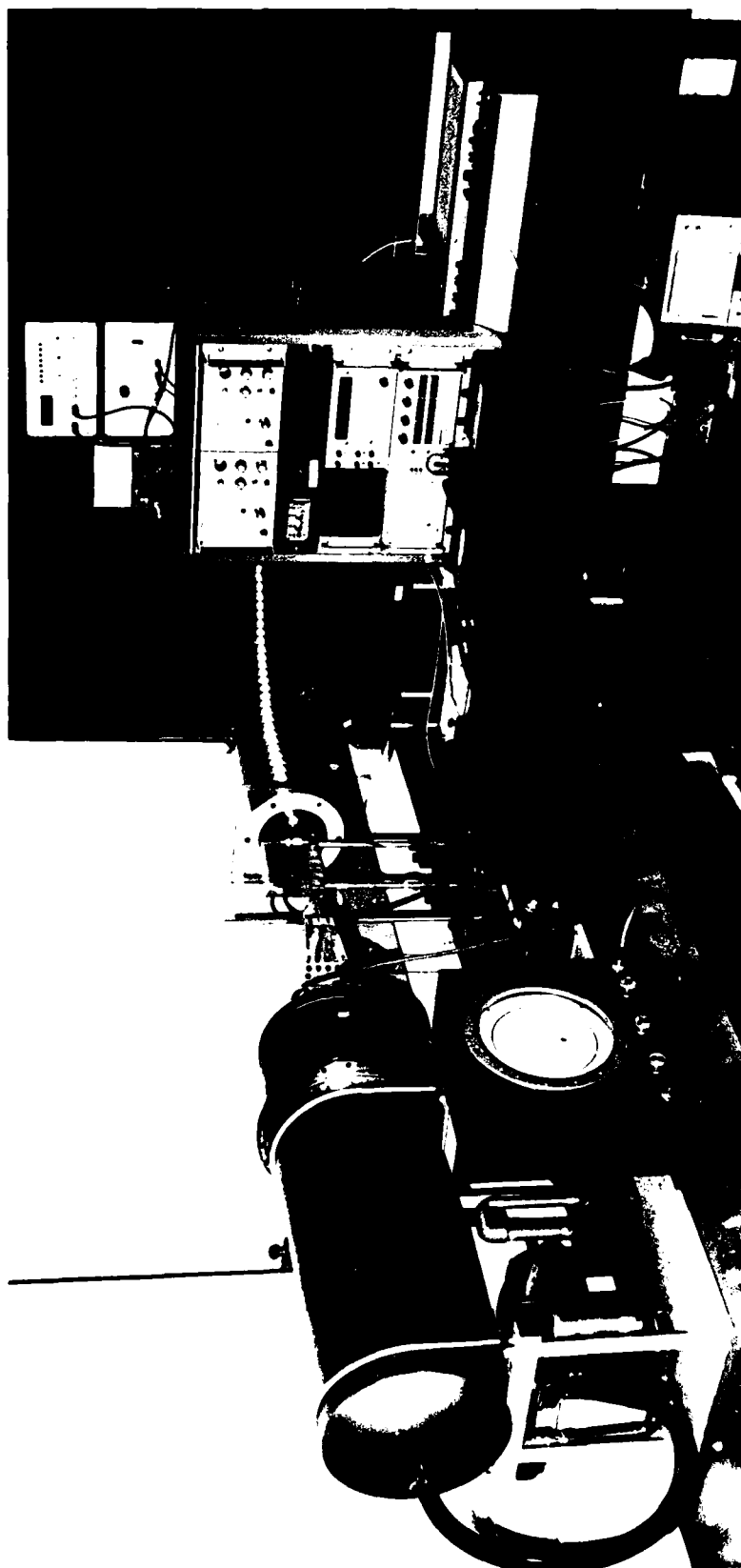


Figure 2

Side view of windtunnel
transition section

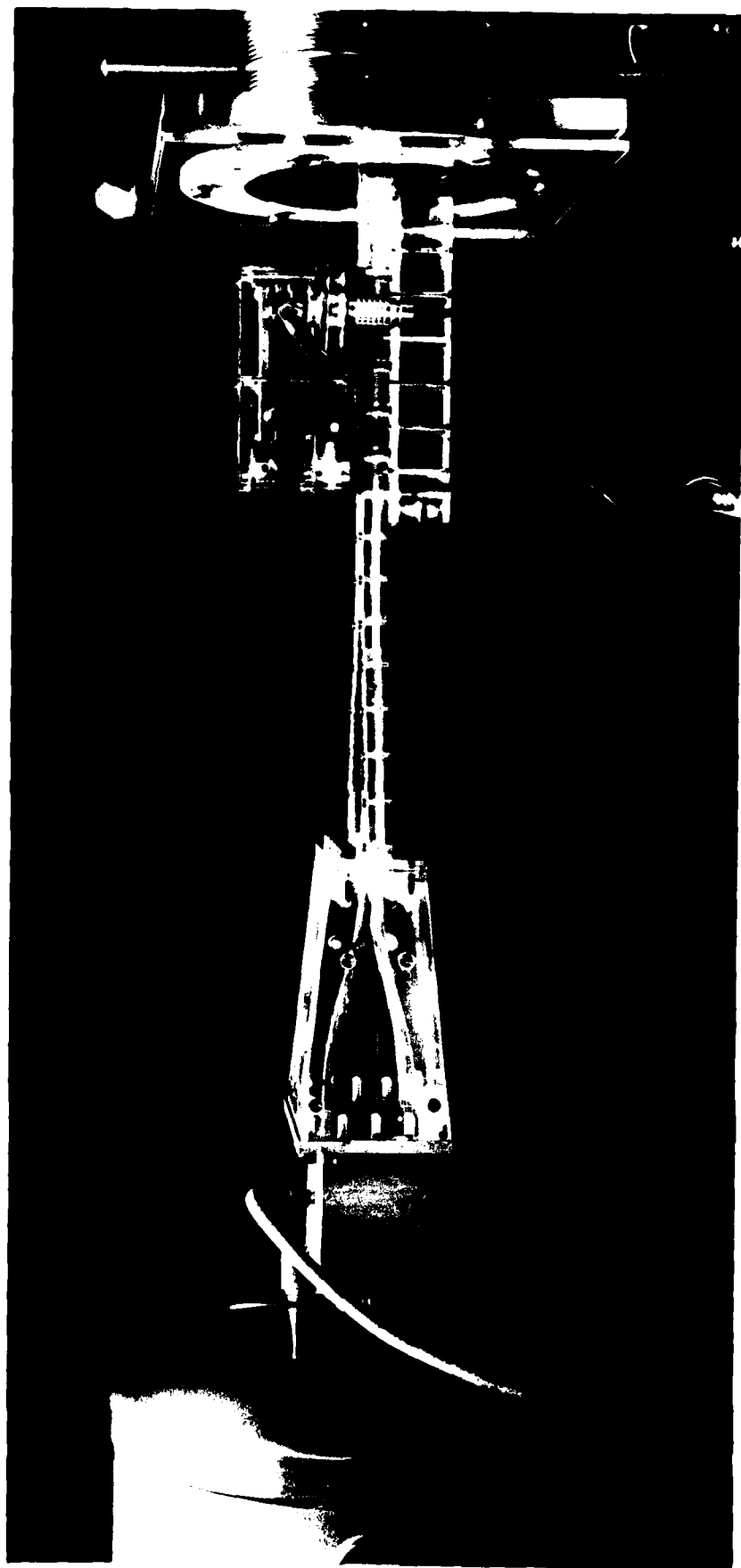
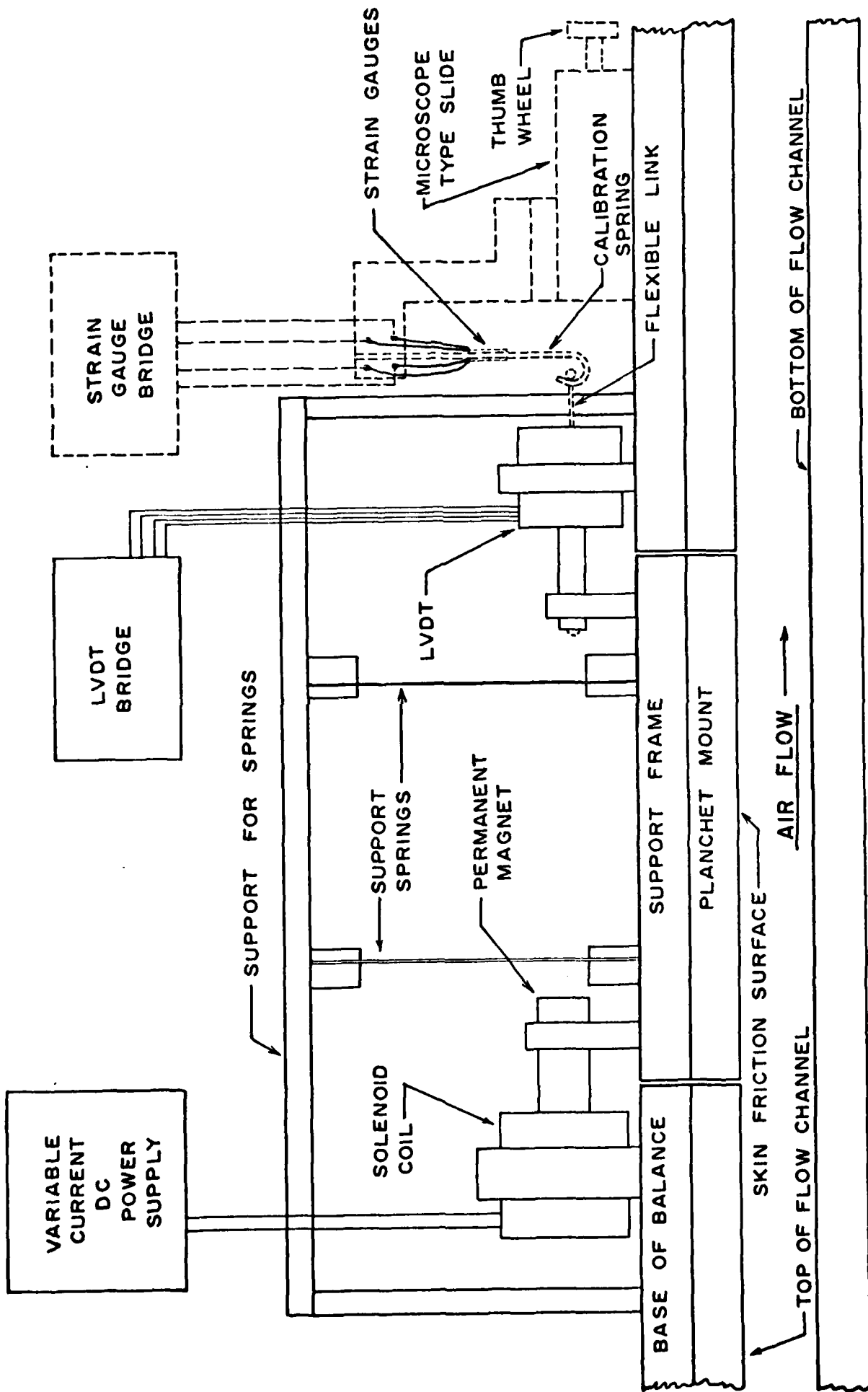


Figure 3

Schematic Diagram of Prototype
Skin Friction Drag Balance



SCHEMATIC OF SKIN FRICTION BALANCE

Figure 4

View of Prototype Skin Friction

Drag Balance

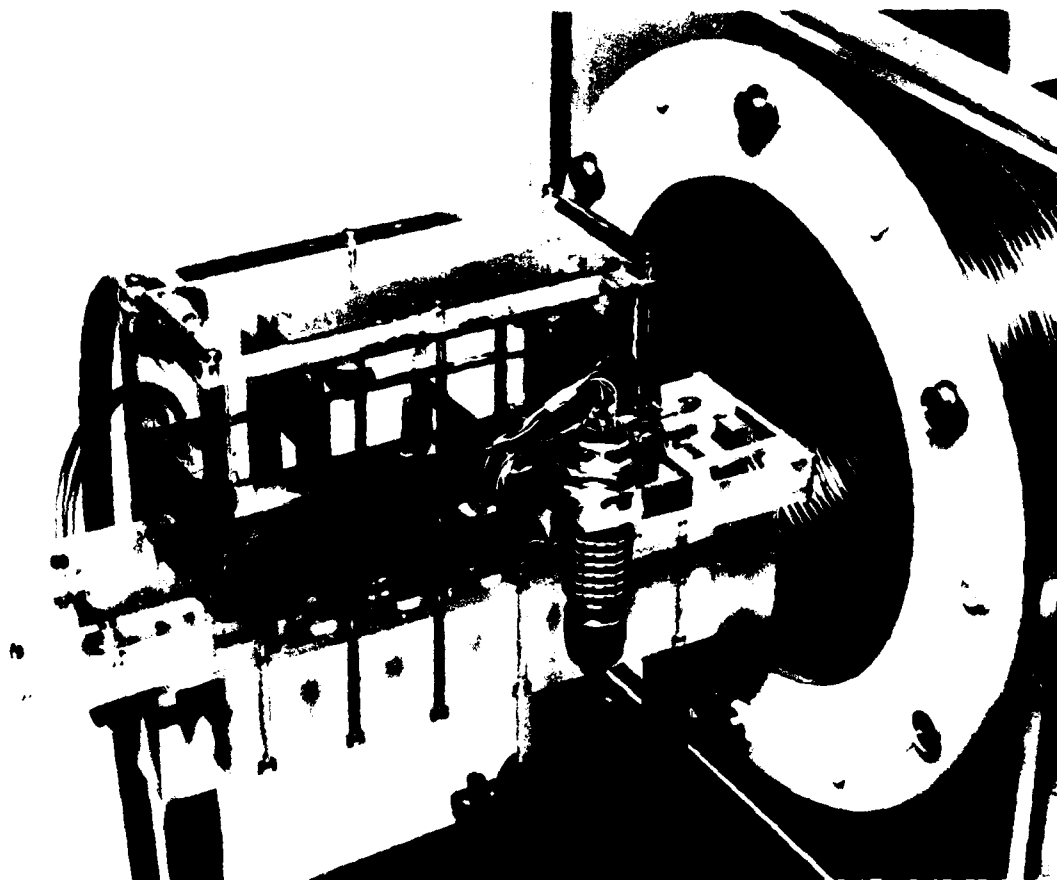


Figure 5

Side View of Calibration
Spring Assembly

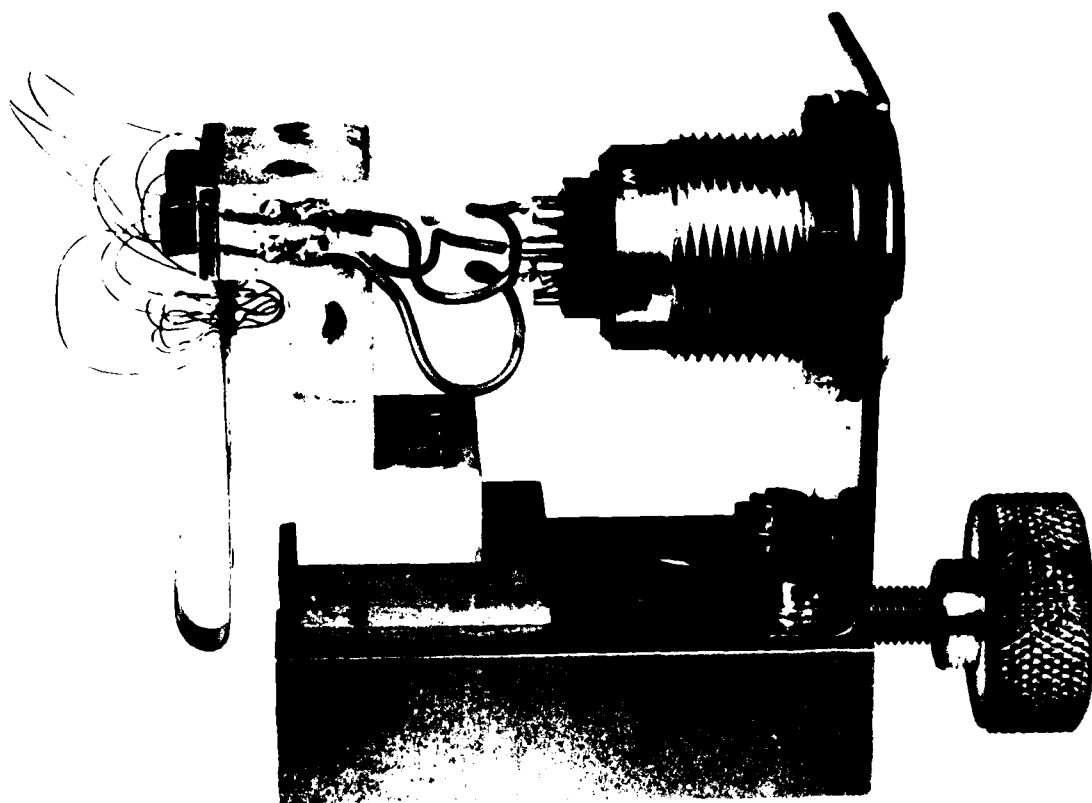


Figure 6

Front View of
Calibration Spring

(x 4)

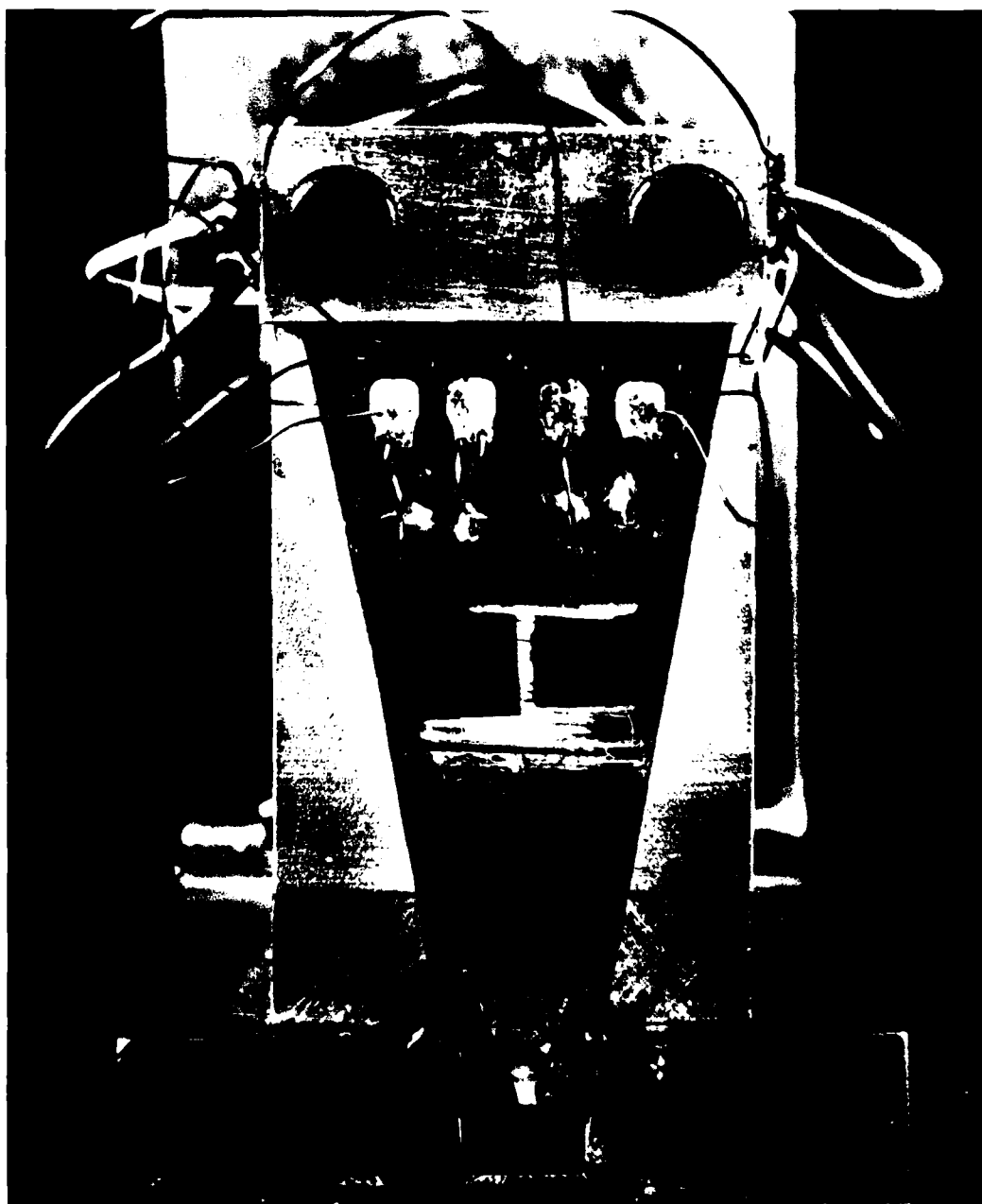


Figure 7

Schematic Diagram of Calibration

Procedure for Spring

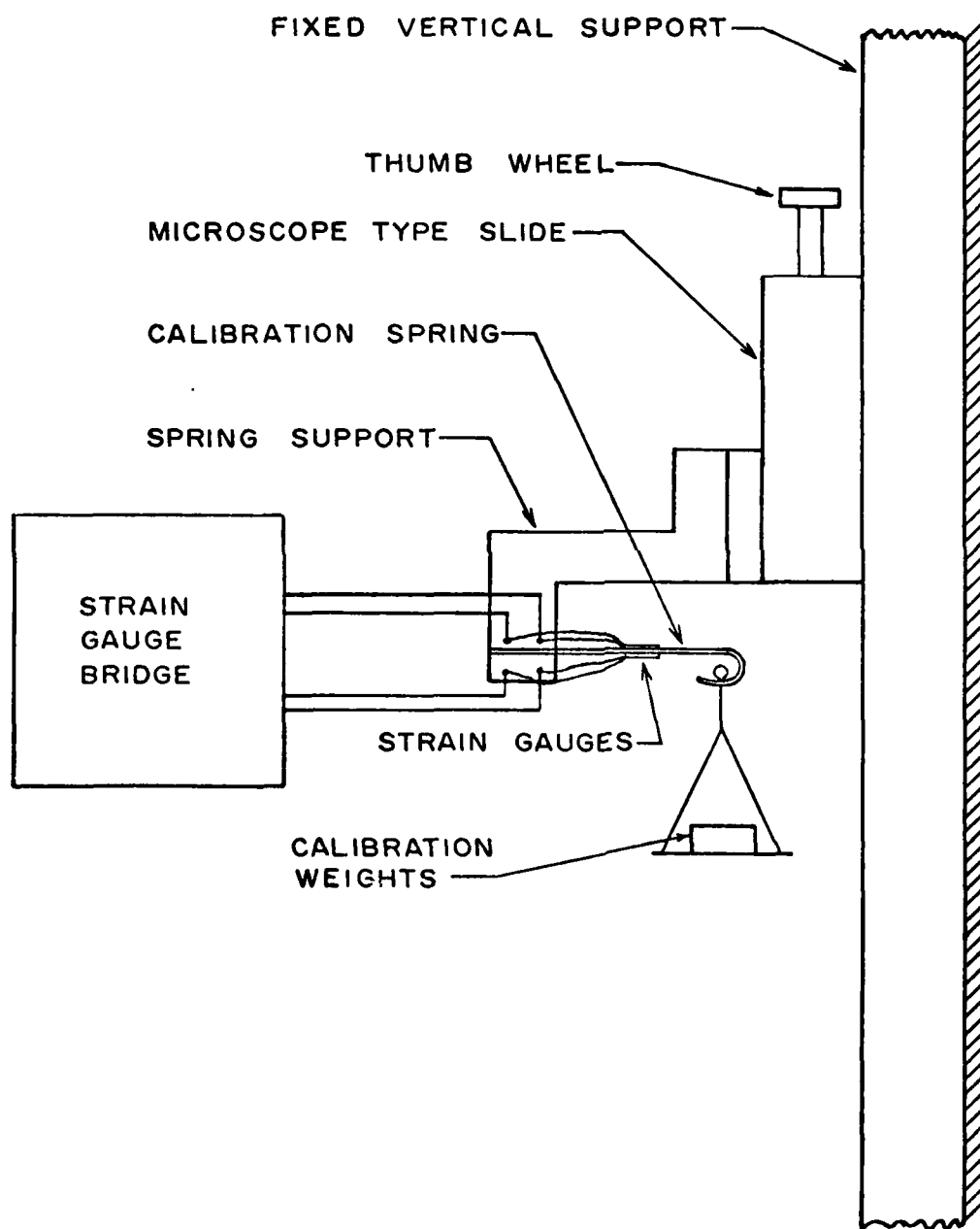
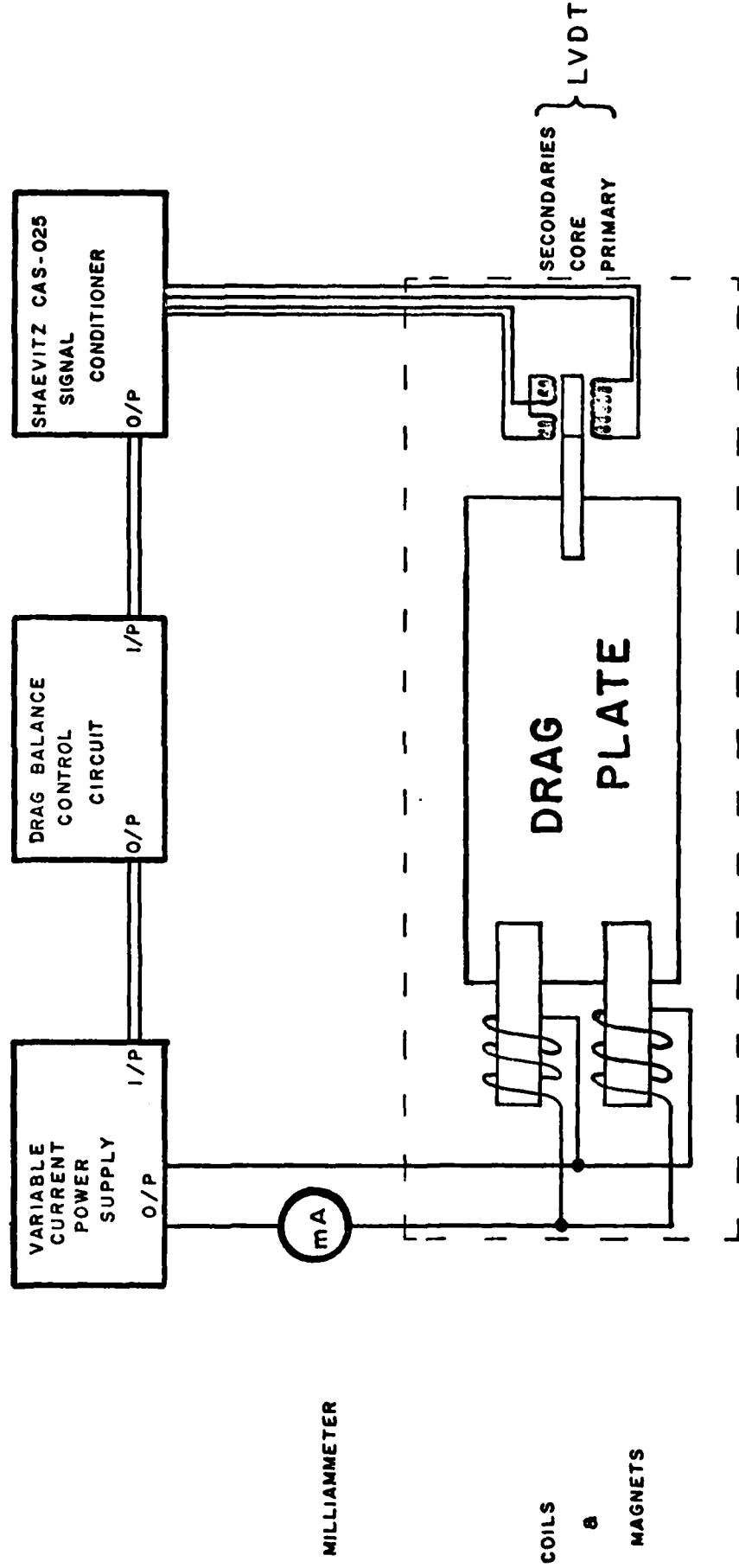


Figure 8

Schematic Diagram of Drag Balance
Automatic Control System

DRAG BALANCE CONTROL SYSTEM



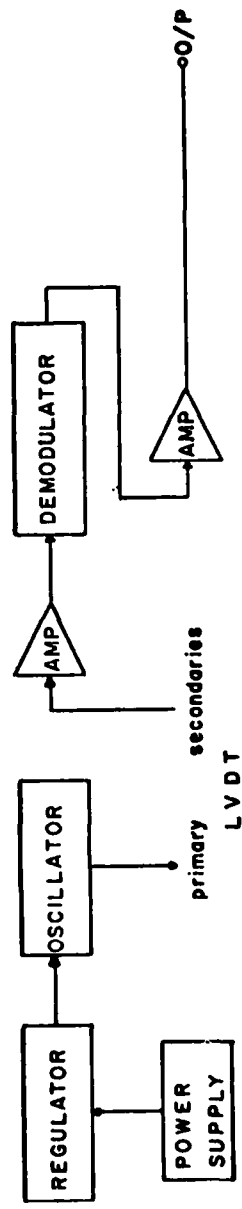
DRAG BALANCE

Figure 9

Schematic Diagrams of Signal Conditioner
and Control Circuit

SCHEMATIC DIAGRAMS OF CONTROL CIRCUIT AND SIGNAL CONDITIONER

SHAEVITZ CAS-025
SIGNAL CONDITIONER



DRAG BALANCE
CONTROL CIRCUIT

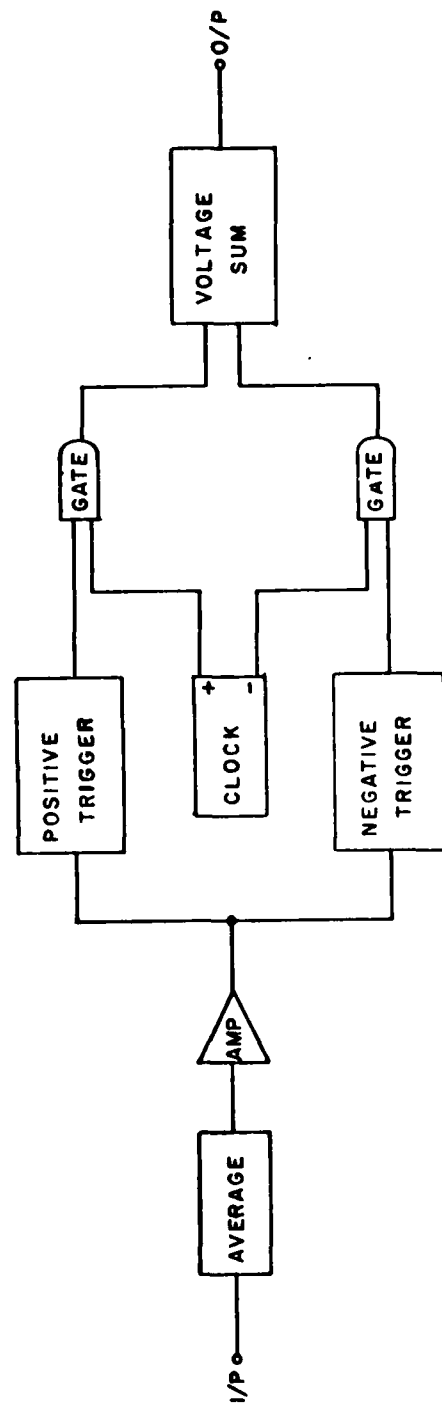


Figure 10

Circuit Diagram of Control Circuit

- 741 Inverting Operational Amplifier
- 555 Timer Chip in Astable Multivibrator Mode
- 4093 Quad 2-Input Schmitt Nand Gates

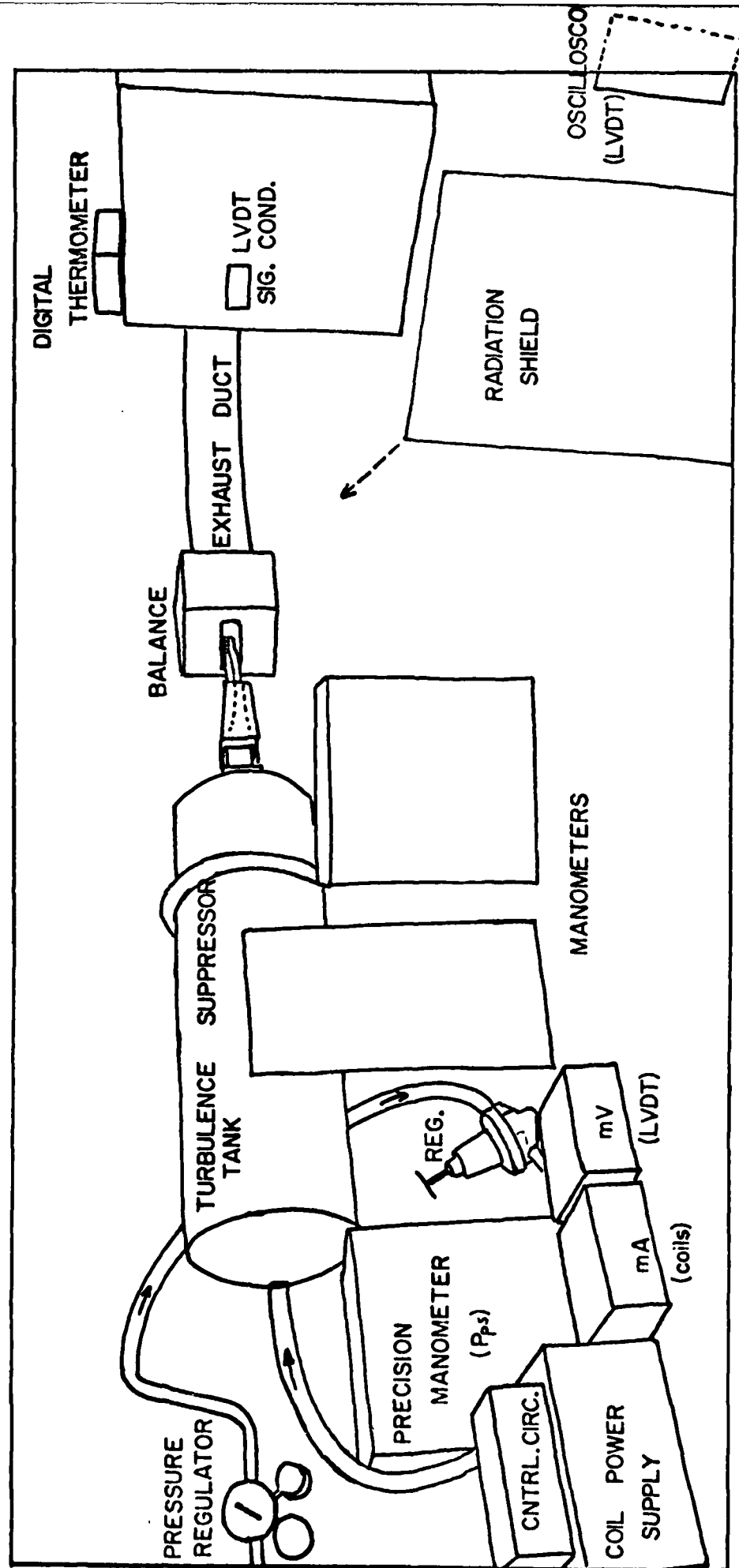
2



Diodes - IN4148 Capacitors - polycarbonate

VIEW OF WINDTUNNEL AND DRAG BALANCE SYSTEM

Figure 11



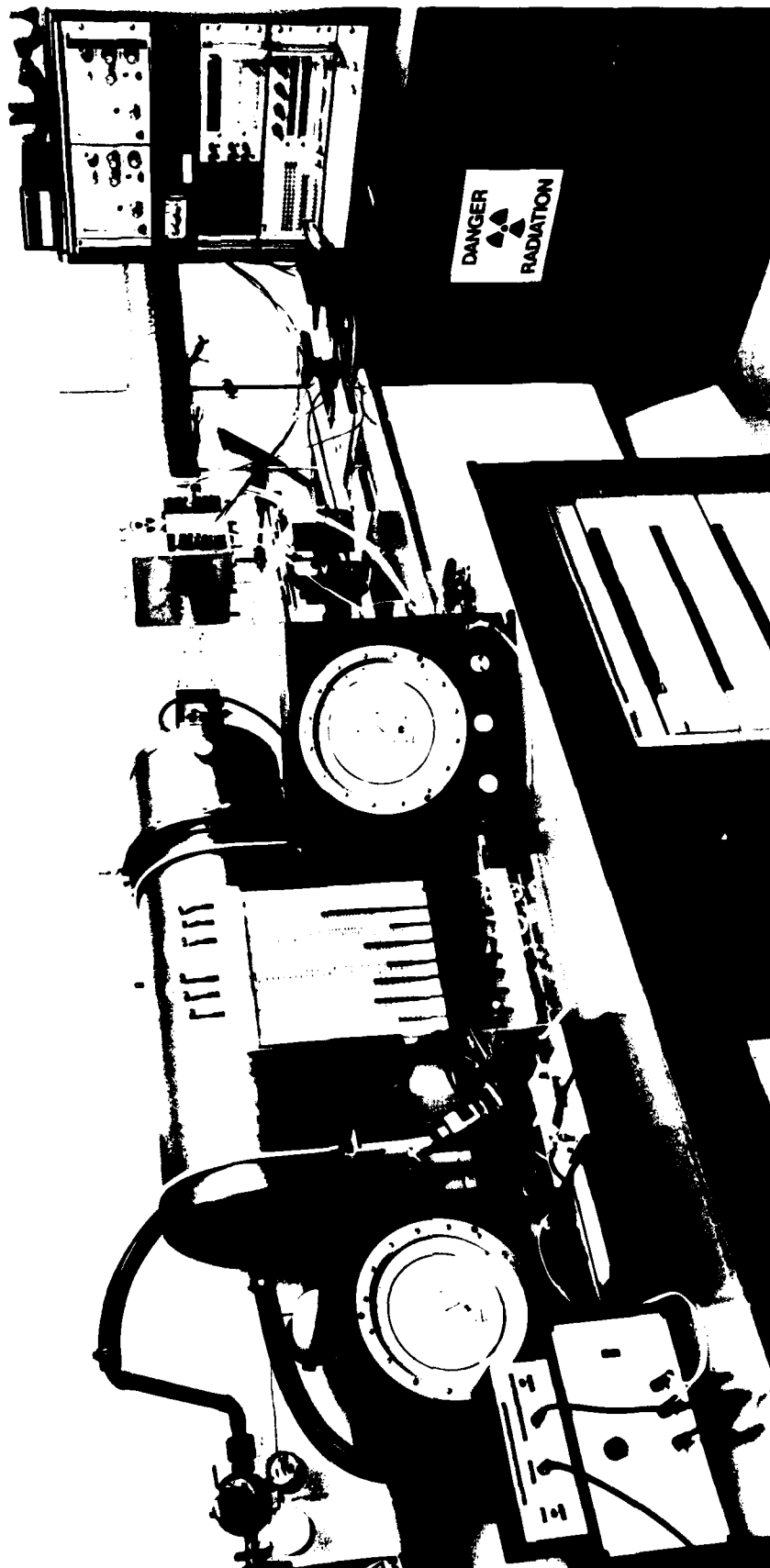


Figure 12

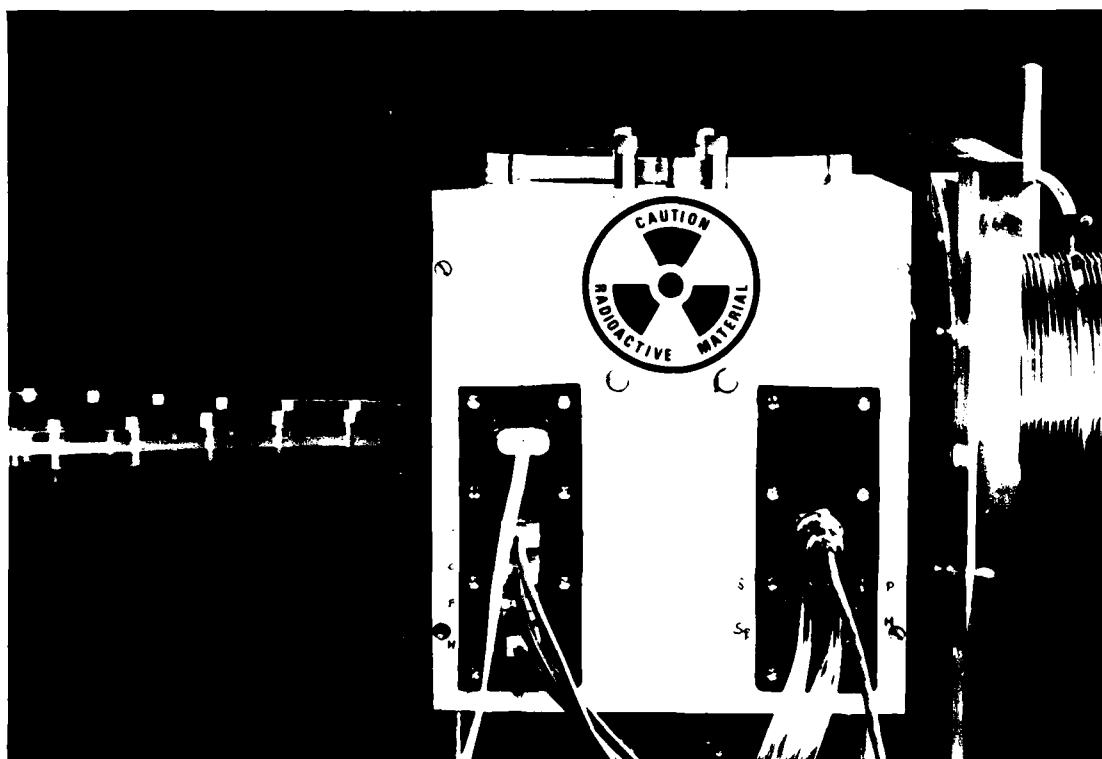
View of Skin Friction Drag Balance

In the left of this picture can be seen the second stage of the windtunnel transition section, leading into the balance.

The two removable panels on the front of the balance are for coil current and thermocouple lead throughs (on the left), and for pressure and LVDT connections (on the right). The top of the right hand panel holds the LED's used in the drag plate levelling process.

The knurled adjusters (two on the lateral faces of the housing, and four top and bottom) are used for tensioning the supporting wires.

The start of the exhaust duct and its pressure tap can be seen in the right hand section of the photograph.



TOP INSIDE VIEW OF BALANCE

Figure 13

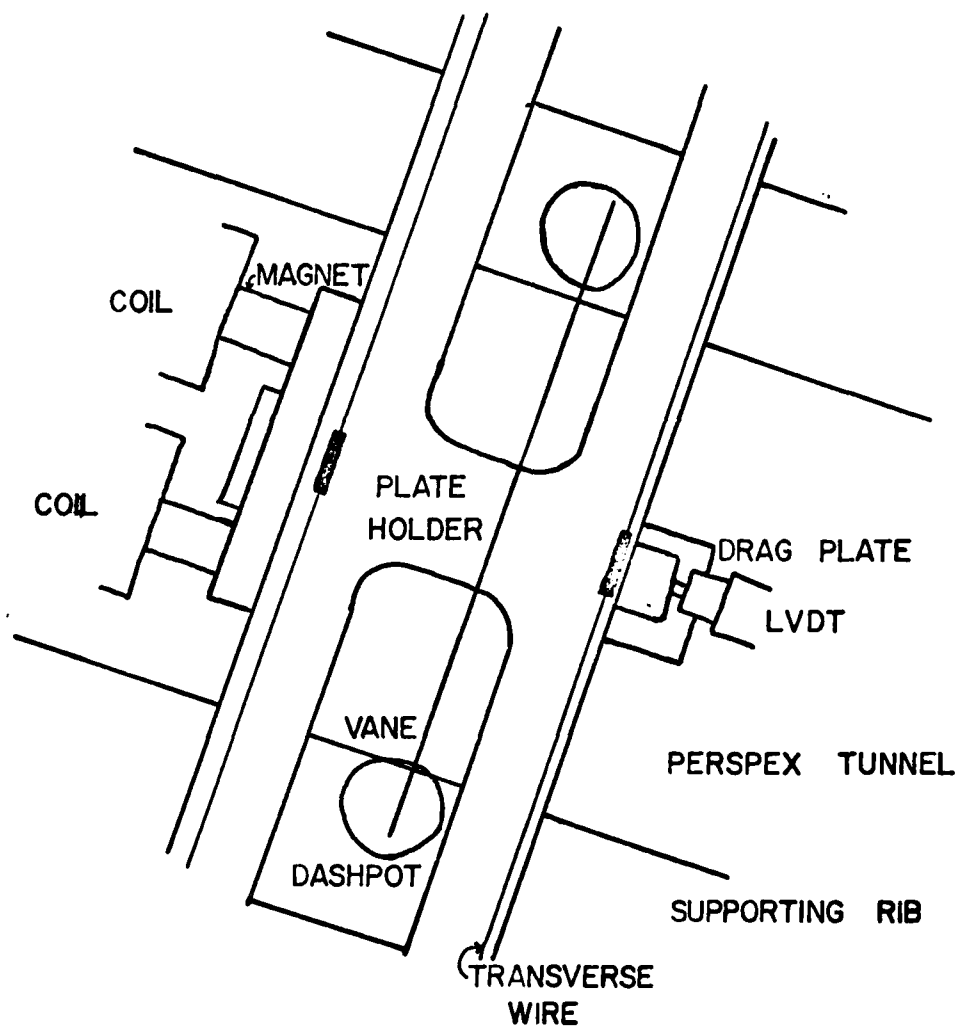




Figure 14

View from below of the inside of
the drag balance

The brass drag plate can be seen through the removable section in the lower windtunnel wall. Beyond the upper surface of the tunnel the H shaped drag plate holder can be seen.

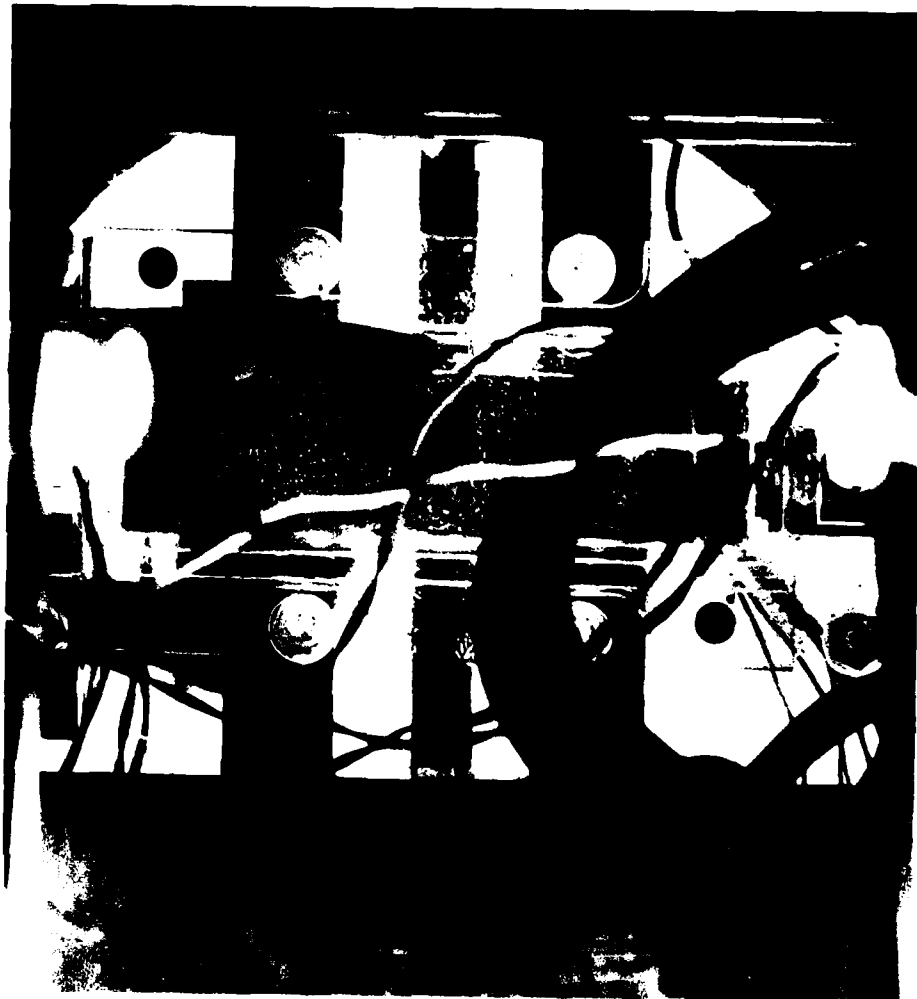


Figure 15

Photograph of Levelling Plate

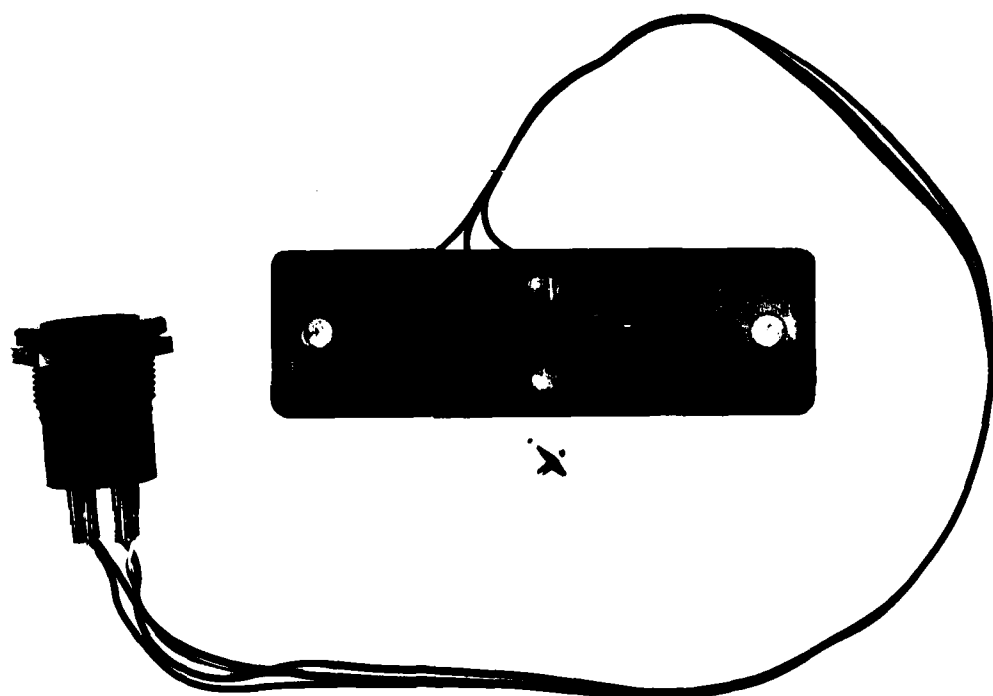
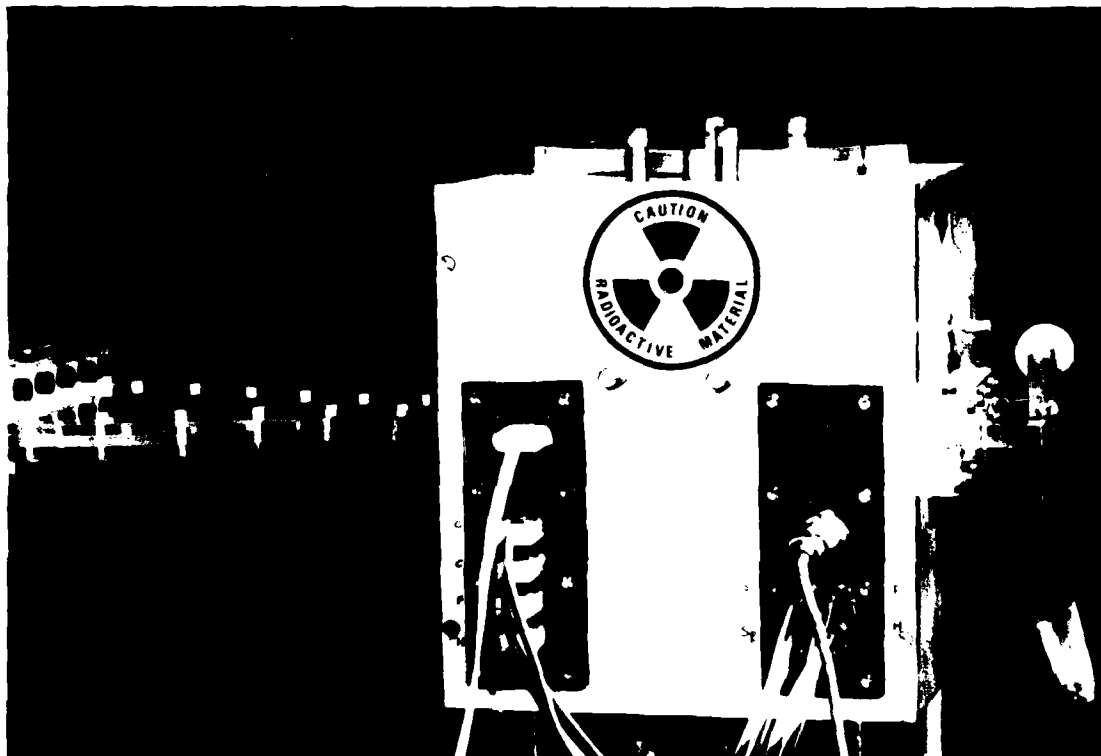


Figure 16

Photograph of Balance During Calibration

The photograph illustrates the ease with which the balance can be calibrated; the exhaust duct is removed, the pulley fixed in place, and the plug in the wall unscrewed. This has the cotton thread attached to the plate holder running through it, and the balance is then ready for calibration. Access to the interior of the balance housing is not needed.



3 Experimental Work

This section describes the experimental work performed, consisting of balance calibrations, obtaining drag curves for a range of flow speeds, and then taking drag data at several sample flow velocities for a range of different drag plates.

The balance was recalibrated and a new drag curve obtained after each plate change. Reproducibility between similar plates is $\sim 1\%$. During the course of the experiments, a check of other experimental parameters, such as temperatures of housing, coils and flow, was maintained, but the small range of variation of these parameters seemed to have no significant effect on either the calibration or the drag data.

In the type of set up used, it is difficult to predict precisely the drag forces to be expected. At high flow velocities, however, i.e. when the boundary layer is thin compared with the channel thickness, it is possible to approximate the situation by a flat plate in a uniform flow* (see fig. 17 overleaf). Here X is the effective entry length of the channel; one might expect $x=0$ to correspond to a point somewhere in the transition section of the windtunnel. u_∞ will be taken to be equal to the centreline velocity, u_0 , of the tunnel near the drag plate.

The local shear stress on one side of the plate is given by¹

$$\tau = 0.332 \sqrt{\mu\rho} u_0^{3/2} / \sqrt{x} .$$

* Assuming that the pressure gradient along the channel is not too great.

The drag on the plate is then

$$D = \int_{\text{plate}} \tau dA = W \int_{x=X}^{X+1} \tau dx = 0.664 W \sqrt{\mu \rho} u_o^{3/2} (\sqrt{X+1} - \sqrt{X}) .$$

Thus the skin friction drag coefficient is given by

$$C_f = \frac{D}{\frac{1}{2} A \rho u_o^2} = \frac{1.328}{\sqrt{R_1}} \left(\sqrt{1 + \frac{X}{1}} - \sqrt{\frac{X}{1}} \right) .$$

For $X=0$, this reduces to the usual Blasius equation for skin friction drag on a plate in uniform laminar flow.

Good agreement with this formula has been reached for $\delta/a < 0.4$; X may be determined from the experimental data and as expected corresponds to an entry length beginning near the centre of the two stage transition.

At lower flow velocities, boundary layers (including those on the side walls) are not small compared with the channel dimensions and it is difficult to predict the relationship between C_f and Re .

3.1 Calibration and Initial Tests of Prototype Balance

Prior to calibration the strain gauge spring was loaded cyclically (to 10 gf in 0.5 gf steps) several times to work out any strains in the gauge cement. Once an acceptably low degree of hysteresis had been achieved rough calibrations were obtained by loading in one direction only. Checks were made on the amount of drift under load; this was found to be acceptable. To estimate the effective tare weight of the

pan and horizontal spring, best-fit power curves were determined for the first six points of each calibration curve for a range of assumed tare weights. The curves of r^2 vs weight gave a "pan load" of 0.30 ± 0.01 gf.

A final set of seven calibrations was then obtained (see fig. 18 for a typical calibration curve) and best-fit power curves of the form

$$R/mV = a_s (1/gf)^{b_s}$$

calculated.

Results were as follows:-

Table 1 Spring Calibration

Calibration Code	a_s	b_s
D1	0.527	0.960
D2	0.534	0.971
D3	0.530	0.971
D4	0.529	0.955
D5	0.540	0.966
D6	0.530	0.975
D7	0.540	0.963

For each calibration $r^2 > 0.9995$.

There was no evidence for an a_s on b_s dependence, a temperature dependence (within the temperature limits encountered), or a dependence

on bridge warm up time, so final values for a_s and b_s are taken as direct averages of the above values, yielding:-

$$a_s = 0.533 \pm 0.002$$

(standard errors)

$$b_s = 0.966 \pm 0.003$$

The calibration of the balance is then performed by establishing an accurately known current in the coil and bringing the LVDT reading to zero using the calibration spring, recording the bridge reading when this had been accomplished. See fig. 19 for a typical calibration curve. In all ten accurate calibrations were performed and best fit power curves obtained:- $R/mV = a_c (I/mA)^{b_c}$.

Results were as follows:-

Table 2 Prototype Balance Calibration

Calibration Code	a_c	b_c
E1	0.0382	0.947
E2	0.0504	0.908
E3	0.0399	0.944
E4	0.0425	0.932
E5	0.0507	0.913
F1	0.0371	0.960
F2	0.0406	0.943
F3	0.0426	0.937
F4	0.0522	0.901
F5	0.0408	0.940

Again $r^2 > 0.9995$ except for F3 (0.998).

These results give

$$a_c = 0.044 \text{ with S.E. } 0.002 \quad b_c = 0.93 \text{ with S.E. } 0.02$$

The final calibration equation has the form

$$1/gf = \alpha (I/ma)^\beta$$

where

$$\alpha = \left(\frac{a_c}{a_s} \right)^{1/b_s} \quad \beta = b_c/b_s$$

Error calculations for α and β are complicated by the dependence of the second calibration on the first and by a correlation between a_c and b_c ($a_c \approx 0.31 - 0.28 b_c$). Results for α and β with estimated errors are

$$\alpha = 0.076 \pm 0.09 \quad \beta = 0.96 \pm 0.02$$

The calibration curve is shown in figure 20. Some initial runs with the balance using zero grade air were then made; the drag curves obtained are shown in figures 21 and 22. At high flow speeds, good agreement is reached with the Blasius type curve; X is found to be approximately 0.23 m.

The behaviour of the C_f vs R_1 curve at $R_1 \sim 10^6$ suggests the flow is becoming turbulent at this point, but due to the limitations of the coil data at higher flow could not be obtained.

3.2 Performance Tests of Automatic Control System

Charts recording plate position and balance control circuit output have been obtained for a range of flow conditions, showing both steady state behaviour and response of the automatic control system (A.C.S.) to changing flow conditions, simulated by setting up a constant flow before switching the circuit on (see figs 23, 24, 25). The oscillations noticeable in the traces for high flow velocities are a consequence of the vibration of the steel exhaust duct. Considering its simplicity, the control circuit exhibits surprisingly good response and stability characteristics, and has been found to be entirely adequate over the whole range of calibration and flow conditions encountered in this work.

3.3 Drag Data Obtained with Prototype Balance and ACS

The data shown in fig. 26 was obtained using the ACS and "wet" air from the compressor. Data was taken mainly over the range in which agreement with the Blasius curve was obtained and also around $R_1 = 10^6$ to see if a transition was again observed. In fact no signs of deviation from the $C_f \propto 1/\sqrt{R_1}$ curve were observed up to the maximum flow velocity attained, ~ 0.8 Mach Number. It is possible that the previous data was inaccurate (difficult to obtain good data without ACS) but it is more likely that a transition to turbulent flow had been taking place, resulting from either slight misalignment of the drag plate, or misalignment of the test section with the first transition section.

The good agreement between the experimental and "theoretical" curves and the degree of reproducibility of results obtained for a given plate configuration (of the order of 1%) indicate that the concept of the drag balance is satisfactory, and a modified balance with better reproducibility between plates should prove to be adequate for drag reduction investigations.

3.4 Calibration and Initial Tests of Drag Balance

Before calibrating the balance, it was decided to determine the resonant frequency of the balance and the effectiveness of the dashpot damping. To do this a 7.5 mV rms signal from a Levell Oscillator was fed into the input socket of the coil power supply. The corresponding LVDT voltage amplitude was measured on an oscilloscope and a plot of amplitude ratio for a range of frequencies obtained (see fig. 27). If we call k/ω_0 the damping factor where k and ω_0 can be defined from the equation of motion:-

$$\ddot{x} + 2k\dot{x} + \omega_0^2 x = 1e^{i\omega t} \quad \text{(the forcing function can have unit amplitude w.l.o.g.)}$$

The amplitude ratio is then

$$A = \frac{1}{\sqrt{1 - \frac{\omega^2}{\omega_0^2} + \frac{4k^2\omega^2}{\omega_0^4}}}$$

and this is a maximum for

$$\omega = \omega_p \text{ given by } \left. \frac{\partial A}{\partial \omega} \right|_{\omega_p} = 0$$

$$\Rightarrow \frac{\omega_p^2}{\omega_o^2} = 1 - \frac{2k^2}{\omega_o^2} .$$

The peak amplitude is then

$$A_p = \frac{1}{(2k/\omega_o) \sqrt{1 - k^2/\omega_o^2}} .$$

It follows that a measurement of A_p and ω_p will give ω_p/ω_o and k/ω_o :-

$$\frac{\omega_p^2}{\omega_o^2} = \sqrt{1 - \frac{1}{A_p^2}}$$

$$\frac{k^2}{\omega_o^2} = \frac{1}{2} \left(1 - \frac{\omega_p^2}{\omega_o^2} \right) .$$

This gives

$$\omega_o \approx 29 \text{ Hz}$$

$$k/\omega_o \approx 0.14 .$$

(The theoretical curve for these values is shown as the dashed curve in fig. 27.)

The damping is some way from optimum but should be adequate. (The resonant frequency will, of course, change if the tensions in the wires are altered, e.g. on changing drag plates, but as the tensions are kept roughly the same the above values may be taken as typical.)

A rough set of drag data was then taken, including measurements

of the static pressures at the plate and pitot tube (see fig. 28).

It can be seen that in calculating the Mach Number of the flow from

$$\left(\frac{P_{ps}}{P_{at} + P_s} \right) = \left(1 + \frac{\gamma - 1}{2} M^2 \right)^{\frac{\gamma}{\gamma - 1}} - 1 ,$$

it is a fair approximation (errors a few % only) to neglect P_s compared with P_{at} (though it cannot, of course, be neglected compared with the pitot pressure).

During this test, the maximum leak pressure recorded was ~ 2 mm Hg at $P_{ps} = 200$ mm Hg. Removing the 4 BA stopper in the hole in the housing wall (for calibration purposes) a leak pressure of ~ 10 mm Hg is obtained. There is thus a sensitive indication of leaks; a maximum leak pressure of ~ 2 mm Hg at $P_{ps} = 200$ mm Hg would seem to be tolerable.

The plate was then accurately aligned, wire tensions checked, and a first accurate set of data taken for a range of flow speeds. During this extended procedure, some drift of the zero current is noticeable. If I_n is the current of the n^{th} reading, N the number of readings, and I_s and I_f the zero currents at the start and finish respectively of the test, the current can be corrected by

$$I_c = I_n - I_s(1 - n/N) - I_f n/N ,$$

assuming the drift is roughly linear with time as readings are taken.

The curve of I_c vs P_{ps} obtained is shown in figure 29. (For better accuracy in drag comparisons, a series of readings are taken at a particular flow velocity, checking the zero before and after each reading. This is done for a sample of six or seven flow velocities.)

The data shows that the balance is working satisfactorily and so a series of accurate calibrations were performed using bearings of weight 0.6970 ± 0.0003 gf (the error is the uncertainty in the average weight, rather than the variation between bearings). A typical calibration curve is shown in fig. 30.

The results were as follows:-

Table 3 First Balance Calibration

<u>Calibration Code</u>	<u>Slope of Curve</u> <u>(mA/bearing)</u>	<u>r²</u>	<u>Coil Constant</u> <u>(gf mA⁻¹)</u>
C0905802	2.829	0.9996	0.2464
C0905803	2.814	0.9987	0.2477
C0905804	2.838	0.9998	0.2456
C0905805	2.813	0.9999	0.2478
C0905806	2.836	0.9998	0.2458
C1205801	2.827	0.9999	0.2465

Mean Coil Constant = 0.2466 gf/mA

Standard Deviation = 0.0009 gf/mA

Standard Error = 0.0004 gf/mA

The accuracy achieved by this quick and simple method is far greater than for the strain gauged spring. (Some slight hysteresis is noticeable on sections of the calibration curves due to the pulley not being absolutely free, but the effect is usually negligible. Occasionally

the pulley becomes a bit "sticky", but cleaning the bearings usually rectifies this.)

Having calibrated the balance, a curve of drag coefficient vs Reynolds Number could be obtained; this is shown in fig. 31. Again, agreement is achieved with the modified Blasius curve at high flow velocities. (The curve is higher than that obtained with the prototype; this is to be expected as the channel is wider and the inlet section has been modified.) A value for X of ~ 0.18 m is determined from the data, $x = 0$ corresponding to a point just downstream of the midpoint of the transition section.

Accurate drag measurements were then made at pitot static pressures of 5, 10, 25, 50, 100, 150, 200 mm Hg corresponding to approximate Mach Numbers of 0.06, 0.14, 0.22, 0.30, 0.42, 0.50, 0.58.

It should be noted that accuracy in reading the coil current is, at low flow speeds, limited mainly by external vibration, giving a resolution in coil current of ± 0.05 mA, or, exceptionally (on Sundays for example!) ± 0.025 mA. A summary of the data obtained is given below (coil currents in mA).

Table 4 First Set of Drag Measurements

P_{ps} /mm Hg 5 Calibra- tion Code	10	25	50	100	150	200
D1205801 0.9	2.1	9.9	19.6	36.3	49.7	61.2
D1205802 0.9	2.1	9.8	19.7	36.5	50.1	61.2
D1205803 0.9	2.1	9.8	19.8	36.7	50.2	61.9
D1205804 1.0	2.0	9.8	19.8	36.7	50.4	61.6
D1205805 0.9	2.2	9.9	19.8	36.6	50.4	61.9
<u>0.9\pm0.05</u>	<u>2.1\pm0.05</u>	<u>9.8\pm0.05</u>	<u>19.75\pm0.05</u>	<u>36.55\pm0.10</u>	<u>50.15\pm0.10</u>	<u>61.55\pm0.15</u>

With a coil constant of 0.2466 ± 0.0004 gf/mA, this gives the following drag values:-

Table 5 First Set of Drag Values

P_{ps} /mm Hg	D/gf
5	0.22 ± 0.01
10	0.52 ± 0.01
25	2.42 ± 0.01
50	4.87 ± 0.02
100	9.01 ± 0.03
150	12.37 ± 0.03
200	15.18 ± 0.04

Except at the lowest flows this should be sufficiently accurate to detect drag changes of a fraction of a percent. As a quick check on reproducibility, the drag plate was changed for a similar plain brass plate and the same procedure followed. The corresponding I vs P_{ps} curve is shown in fig. 32.

Four calibrations were then performed as follows:-

Table 6 Second Balance Calibration

Calibration Code	<u>Slope of Curve</u> (mA/bearing)	r^2	<u>Coil Constant</u> (gf mA ⁻¹)
C1805801	2.826	0.9999	0.2467
C1805802	2.820	0.9999	0.2472
C1905801	2.833	0.9999	0.2461
C1905802	2.839	0.9999	0.2455

Mean Coil Constant = 0.2464 gf/mA

Standard Deviation = 0.0009 gf/mA

Standard Error = 0.0004 gf/mA

This is consistent with an unchanged calibration.

A rough set of drag measurements were then taken yielding the data below:-

Table 7 Second Set of Drag Measurements (D1905801)

P_{ps} /mm Hg	5	10	25	50	100	150	200
I/mA	0.9±0.05	2.05±0.05	9.8±0.1	19.7±0.1	N/A	48.4±0.5	61.8±0.5

giving drag values of:-

Table 8 Second Set of Drag Values

P_{ps} /mm Hg	D/gf
5	0.22 ± 0.01
10	0.51 ± 0.01
25	2.41 ± 0.02
50	4.85 ± 0.03
100	N/A
150	11.9 ± 0.1
200	15.2 ± 0.1

Except for $P_{ps} = 150$ mm Hg this is in good agreement with the first set of values. This suggests, as expected, that the major problem in working with the radioactive sources will be attaining a sufficiently accurate drag plate surface.

As a preliminary experiment, it was decided to investigate the effect of the sources when mounted on the opposite wall to the drag plate. Although the irradiation of the boundary layer on the plate will be less, 5 mm of air should not cut the radiation level too greatly in the case of the α and β sources. The β^+ , γ source will give essentially the same level of γ radiation at the plate, but the positrons will be stopped within a very short distance of the source.

The surface roughness of the active plate is, of course, less critical in this configuration, so although the activity at the drag

plate may be lowered the ultimate resolution of the balance is achieved.

The construction of the radioactive drag plates is described in the next section, and the results of this initial investigation in the subsequent section.

3.5 Construction of Radioactive Drag Plates

The ideal approach to the construction of active drag plates would involve taking a standard plate and coating it with a thin film of a radioactive isotope. Unfortunately, at present, this is a prohibitively expensive procedure. Accordingly, standard "static eliminator" radioactive foils, obtained from the Radiochemical Centre at Amersham, have been incorporated into the drag plates. The specifications of the radioactive foils used are given in Table 9.

The polonium and promethium isotopes are sealed onto a substrate by a thin ($\sim 3 \mu\text{m}$) protective coating of silver. The cobalt is infused directly into a copper strip. For use in the drag balance, the foils are incorporated into a drag plate of standard dimensions in such a way as to give an accurately flat, clean surface. The plate is milled out over an area slightly greater than that of the foil^{*}, and the foil is then cemented into the plate using beeswax (supplied from a dental laboratory). This is a surprisingly strong and versatile adhesive; it has the advantages that when molten it flows readily and is transparent (allowing a check on the position of the foil), when set it is extremely

*Note that the ^{210}Po foil was trimmed slightly before use.

Table 9 Specifications of Radioactive Foils

Isotope	Radiation	Activity/mCi	Max. Energy of Particles /MeV	Half-Life	Overall Size/mm ²	Active Area/mm ²
²¹⁰ Po	α	5.5 (Feb. '80)	5.30	138d	70 x 20	60 x 11
¹⁴⁷ Pm	β	120 (Apr. '80)	0.22	2.6a	70 x 17	60 x 10
⁵⁸ Co	β^+ (γ)	10 (Apr. '80)	0.47	71d	70 x 17	60 x 10

hard and rigid (although somewhat brittle), but may easily be softened and removed if the foil position is unsatisfactory.

Initially the foil, typically ~ 0.5 mm thick and slightly curved, is fixed to an accurately flat brass backing strip, ~ 3 mm thick, using double-sided sticky tape. The foil and milled plate are then placed on a flat surface, consisting of greaseproof paper fixed to a flat glass block with double sided sticky tape and then wiped with 3 in 1 graphited oil. The oil soaked paper prevents wax getting onto the surface of the foil, and permits easy release of the plate from the surface once the wax has set.

The outer section of the plate is clamped to the block by spring clips and the foil is then aligned and clamped by screwing five screws through the back of the milled plate and onto the backing strip. The assembly is then carefully warmed with a blowtorch and molten beeswax run into the plate through holes cut in the back. (A diagram showing the plate during the foil mounting procedure is given in fig. 33. A photograph showing the working area used and a plate during construction can be seen in fig. 34. It should be noted that all manipulation of the foils is performed wearing gloves and glasses, and that, where possible, the foils are handled with tongs behind a lead screen having a lead glass window in it. A film monitoring badge is always worn; no dosage greater 0.02 rem/month has been recorded. Particular care is taken not to damage the protective surface of the foils, especially the alpha foil, ^{210}Po being extremely hazardous if ingested.)

The melting point of the beeswax is $\sim 70^{\circ}\text{C}$ and the maximum foil temperature reached during mounting is probably $\sim 100^{\circ}\text{C}$, which should be perfectly safe. Once the wax has set hard (after about 3/4 hour) the clamping screws are removed and the drag plate released from the surface and wiped clean.

Two silver foils and the alpha and beta foils have so far been mounted. Except for the alpha foil the standard of surface achieved has been good. In the case of the alpha foil, the ends of the foil have been capped, making it hard to get a flat surface, and on releasing from the surface one cap partly unfolded. It has not been possible to refix this satisfactorily, so this plate has a slight protrusion at one end. Figure 35 shows one of the silver drag plates in the holder used for the experiment described in the next section.

3.6 Effect of Boundary Layer Irradiation

In this section, an account of a preliminary investigation into the effect of boundary layer irradiation is given. It seems obvious that the drag balance will be less sensitive to surface imperfections on the wall opposite to the drag plate, than to those on the drag plate itself. It follows that one of the radioactive plates could be rapidly mounted, to a reasonably high accuracy, in the lower wall of the windtunnel. The possible loss in accuracy is compensated for by the reduced exposure to the source. There will also, of course, be a drop in the radiation level at the drag plate, but for a 5 mm thick airflow this should not, except perhaps for the alpha source, be too great.

Accordingly, as a preliminary experiment, the active drag plates have been mounted flush with the lower windtunnel surface, opposite to a plain brass drag plate, and drag measurements made at several flow speeds. Each plate is mounted in turn, and three complete sets of drag measurements taken each time. The results are given in Table 10.

Each experiment involves measuring the zero current, drag current,

Table 10 Drag Measurements with Active Plates

Drag values in mA coil current. Calibration is approximately 0.246 gf/mA.

Expt. Code	Drag Plate Type	P _{PS} =5	10	25	50	100	150	200 mm Hg
RD01	Ag#1	0.6	1.55	9.7	19.2	33.4	45.3	56.0
RD02		0.6	1.6	9.8	19.3	33.6	45.8	53.5
RD03		0.6	1.6	9.7	19.3	33.6	46.0	57.0
RD04	Ag#2	0.45	1.75	9.5	19.3	33.6	45.1	55.3
RD05		0.5	1.75	9.6	19.5	34.0	45.2	55.5
RD06		0.5	1.75	9.65	19.5	34.1	45.4	55.4
RD07	¹⁴⁷ Pm	0.3	1.4	8.9	18.3	31.7	42.8	53.0
RD08		0.35	1.4	8.9	18.3	31.8	42.8	52.5
RD09		0.4	1.4	8.9	18.3	31.7	42.8	52.9
RD10	Ag#1	0.5	1.4	9.4	19.0	32.9	44.6	55.1
RD11		0.45	1.45	9.3	19.0	33.0	44.5	55.0
RD12		0.5	1.6	9.4	19.0	33.1	44.6	54.9

zero current, drag current and then zero again, for each flow velocity and then obtaining the average drag current. The measurements are taken in quick succession, but changes in flow velocity are made sufficiently slowly for the plate displacement to be minimal, imposing no undue stresses on the suspension system. The mean drag values for each type of plate have been calculated and are given below:-

Table 11 Mean Drag Values

Plate Type	$P_{PS}=5$	10	25	50	100	150	200 mm Hg
Ag#1	0.6	1.6	9.7	19.3	33.5	45.7	55.5
Ag#2	0.5	1.75	9.6	19.4	33.9	45.2	55.4
^{147}Pm	0.35	1.4	8.9	18.3	31.7	42.8	52.9
Ag#1	0.5	1.5	9.4	19.0	33.0	44.6	55.0

The data taken with the silver plates gives an idea of the spread of values to be expected due to variations in the accuracy of the plate surface and of the positioning in the windtunnel wall. If we assume similar uncertainties apply to the results for the ^{147}Pm foil then values for the drag reduction with the ^{147}Pm plate can be calculated together with rough error estimates. These values are summarised below, and will be discussed in Section 5. Note that the values at $P_{PS}=200$ mm Hg seem surprisingly accurate; this is because the air compressor is delivering almost its full capacity and so the inlet pressure at the flow regulators changes only slowly.

Table 12 Summary of Results

$P_{PS}/\text{mm Hg}$	Approx. Mach Number	Drag Values with Ag Plate	Drag Values with ^{147}Pm Plate	% Decrease in Drag with ^{147}Pm Plate
5	0.06	0.55 ± 0.05	0.35 ± 0.05	(40 ± 20)
10	0.14	1.6 ± 0.1	1.4 ± 0.1	(15 ± 15)
25	0.22	9.6 ± 0.2	8.9 ± 0.2	7 ± 4
50	0.30	19.2 ± 0.2	18.3 ± 0.2	5 ± 2
100	0.42	33.5 ± 0.5	31.7 ± 0.5	5 ± 3
150	0.50	45.2 ± 0.6	42.8 ± 0.6	5 ± 3
200	0.58	55.3 ± 0.3	52.9 ± 0.3	4 ± 1

A few rough results taken with the ^{210}Po foil, which has a poor surface with a slight protrusion at one end, gave increases in apparent drag of $\sim 2\%$, of the order of the uncertainty of the experiment, and little significance is attached to this result.

Figure 18

Typical Calibration Curve for
the Strain Gauge Spring

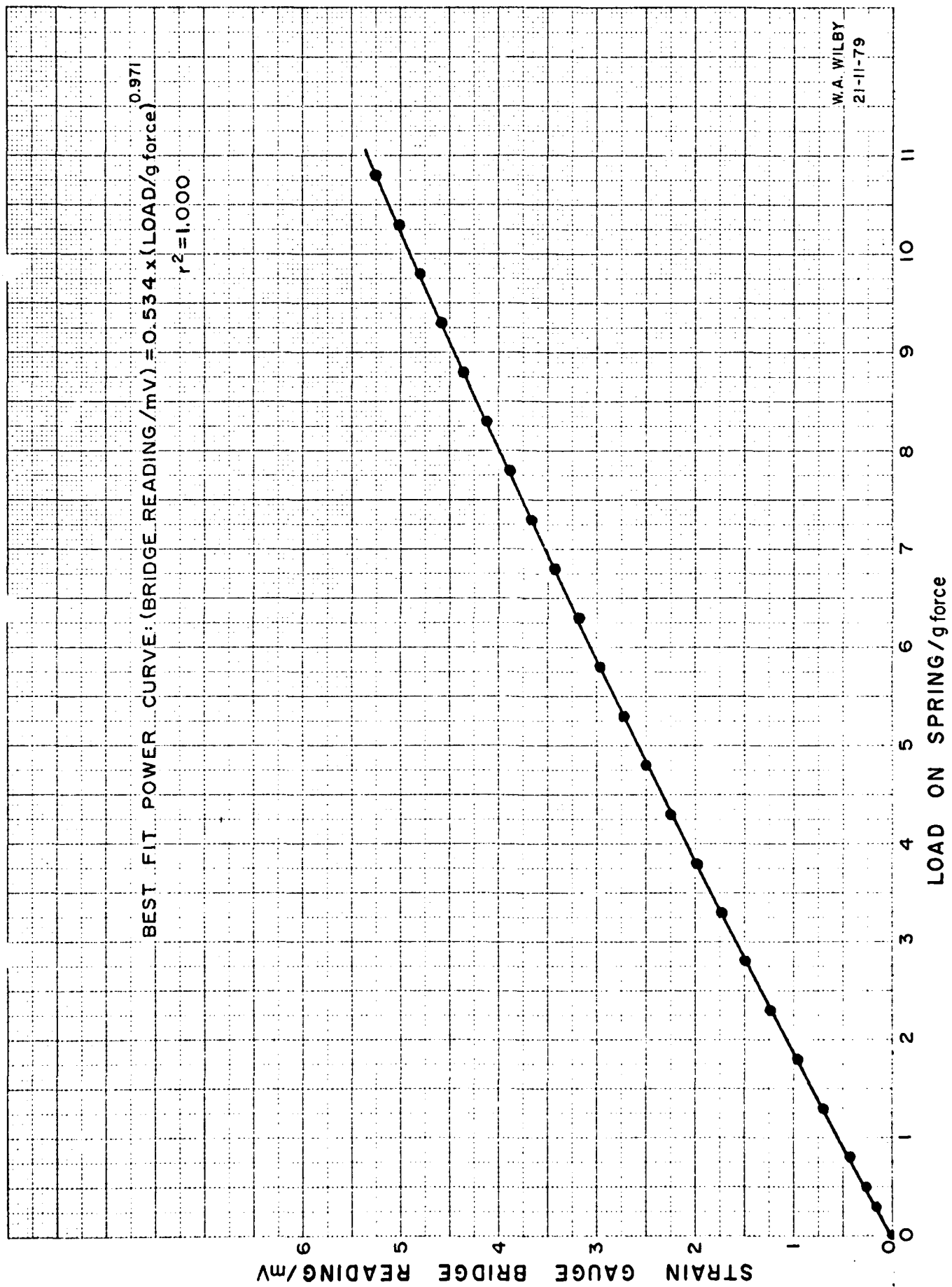


Figure 19

Typical Calibration Curve of Prototype Drag Balance
using Strain Gauged Spring

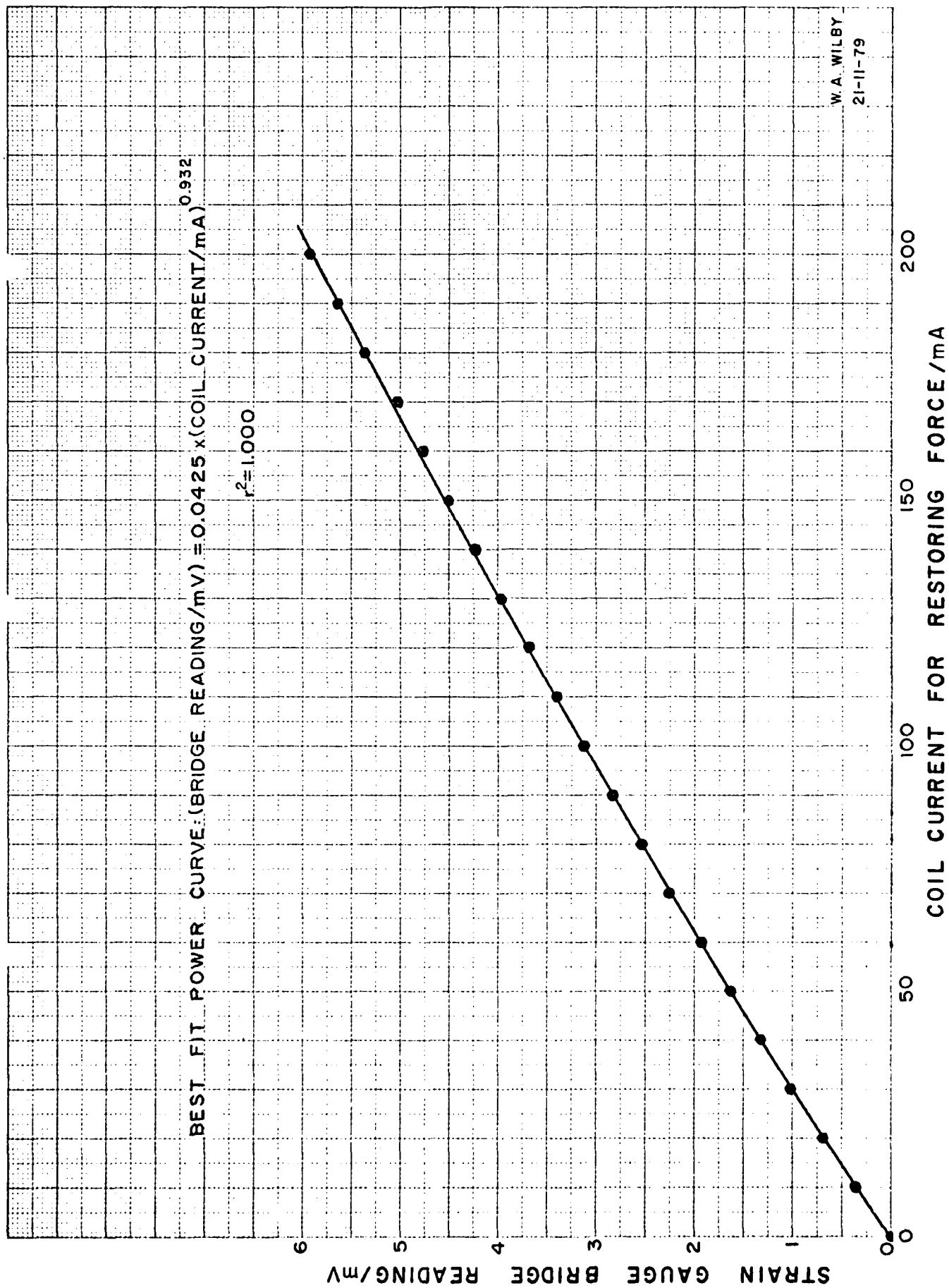


Figure 20

Final Calibration of Prototype Drag Balance

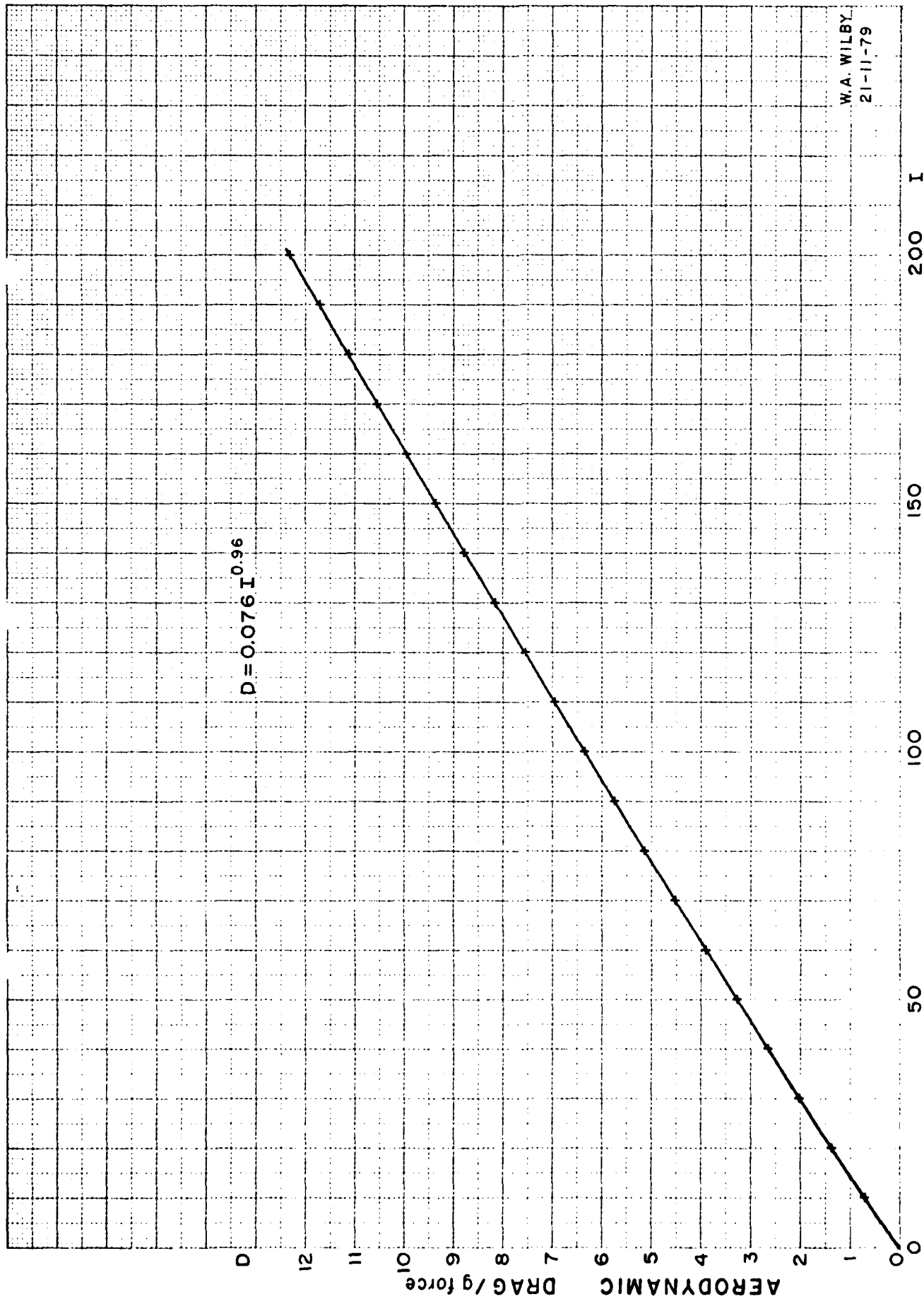
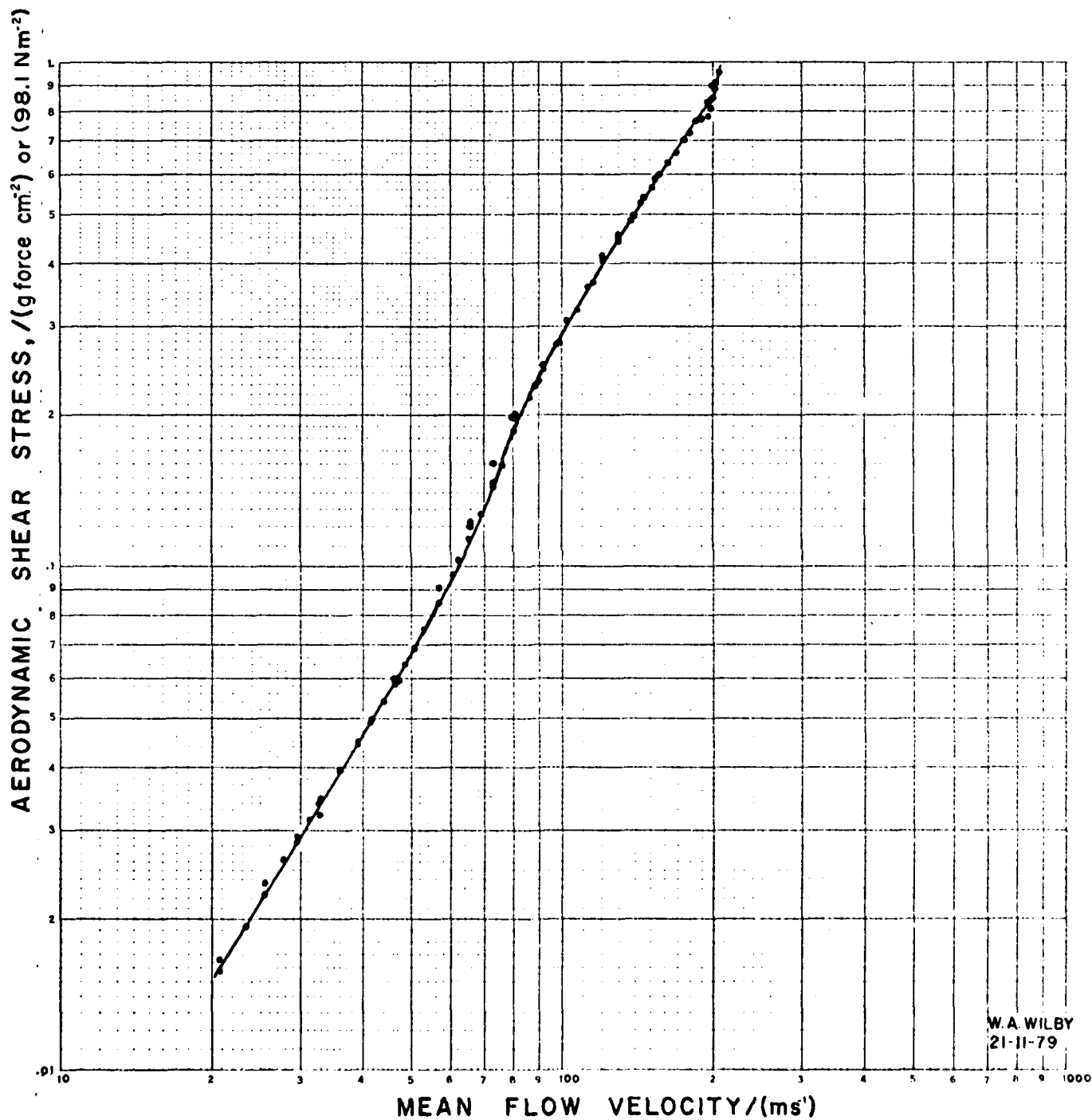


Figure 21

Shear Stress vs Flow Velocity

Preliminary Test using Zero Grade Air



SKIN FRICTION SHEAR STRESS VERSUS AIR FLOW VELOCITY

Figure 22

Drag Coefficient vs Reynolds Number

as fig. 21

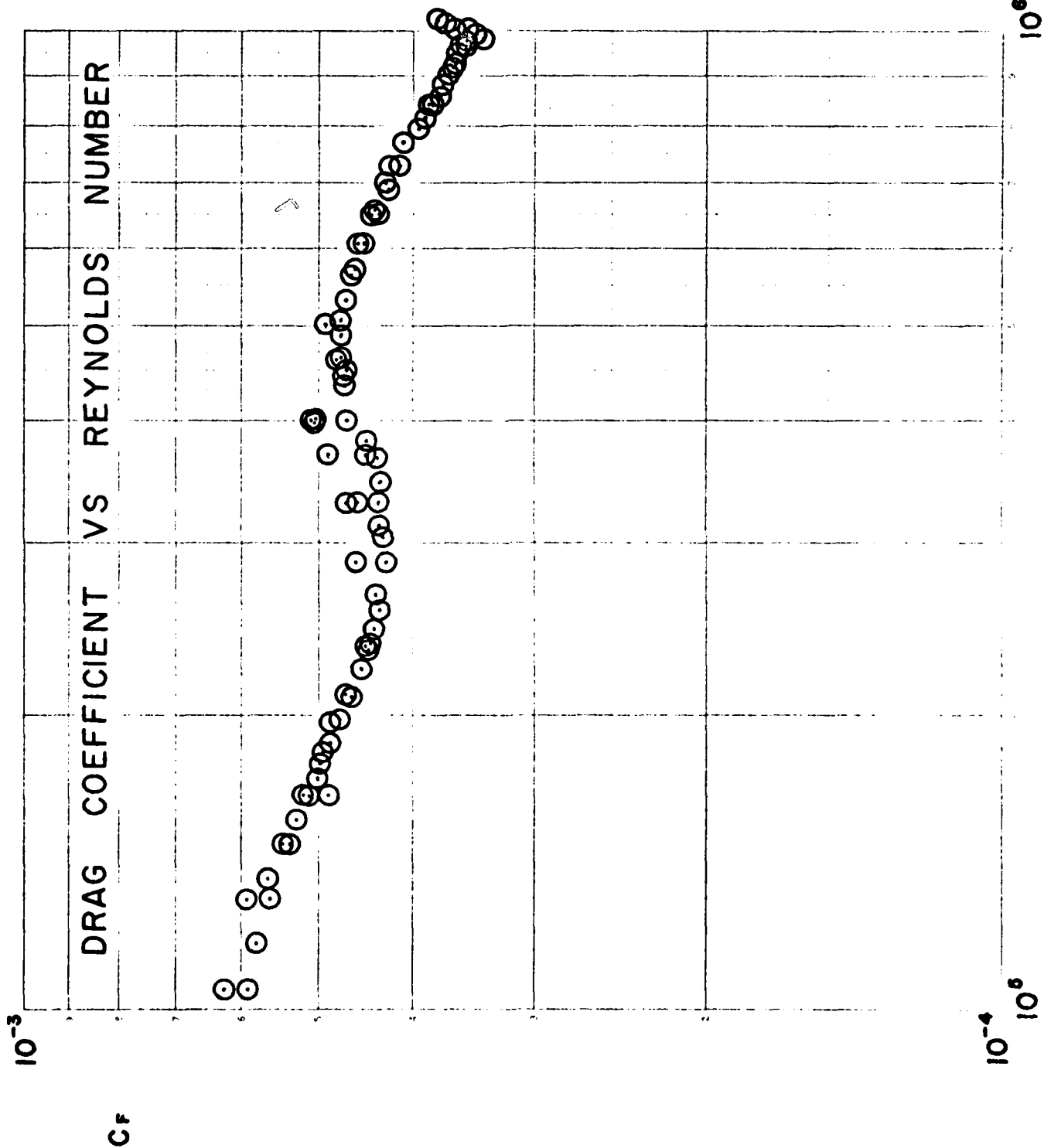


Figure 23

Control Circuit Output for a Range of Trigger Conditions

Inputs causing either positive, negative or no triggering were fed to the control circuit to simulate the application of simple forces to the drag plate.

The output voltage of the control circuit was recorded as a function of time.

The circuit was connected to the coil power supply during this experiment.

The staircase structure of the output is, of course, too fine to be resolved in this way. (Use of an X-Y plotter would seem to be an obvious way of recording this, but the excessively low input impedance of the plotter causes misleading results.)

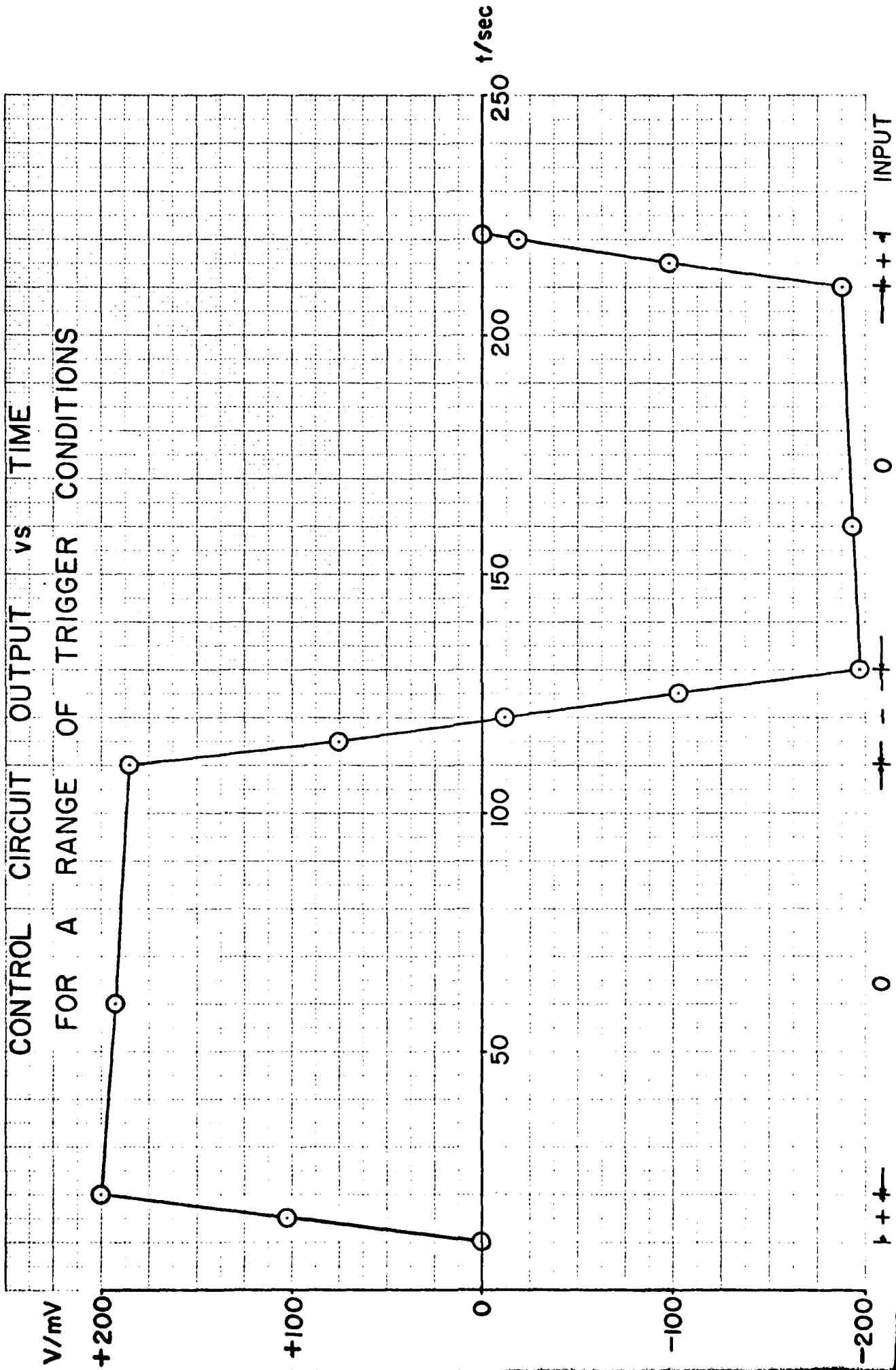


Figure 24

Response Curves for the
Drag Balance Control System

RESPONSE CURVES FOR DRAG BALANCE CONTROL SYSTEM

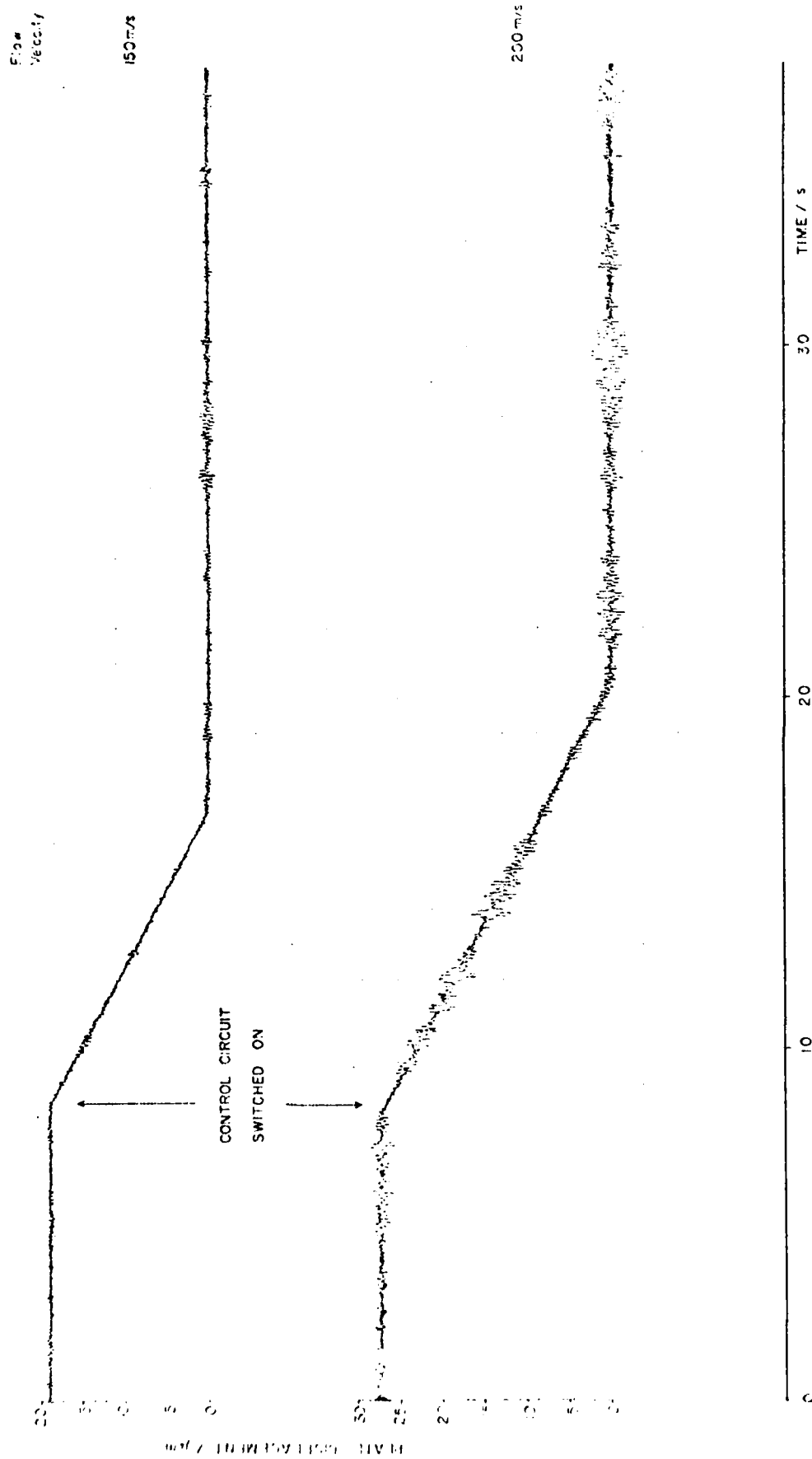
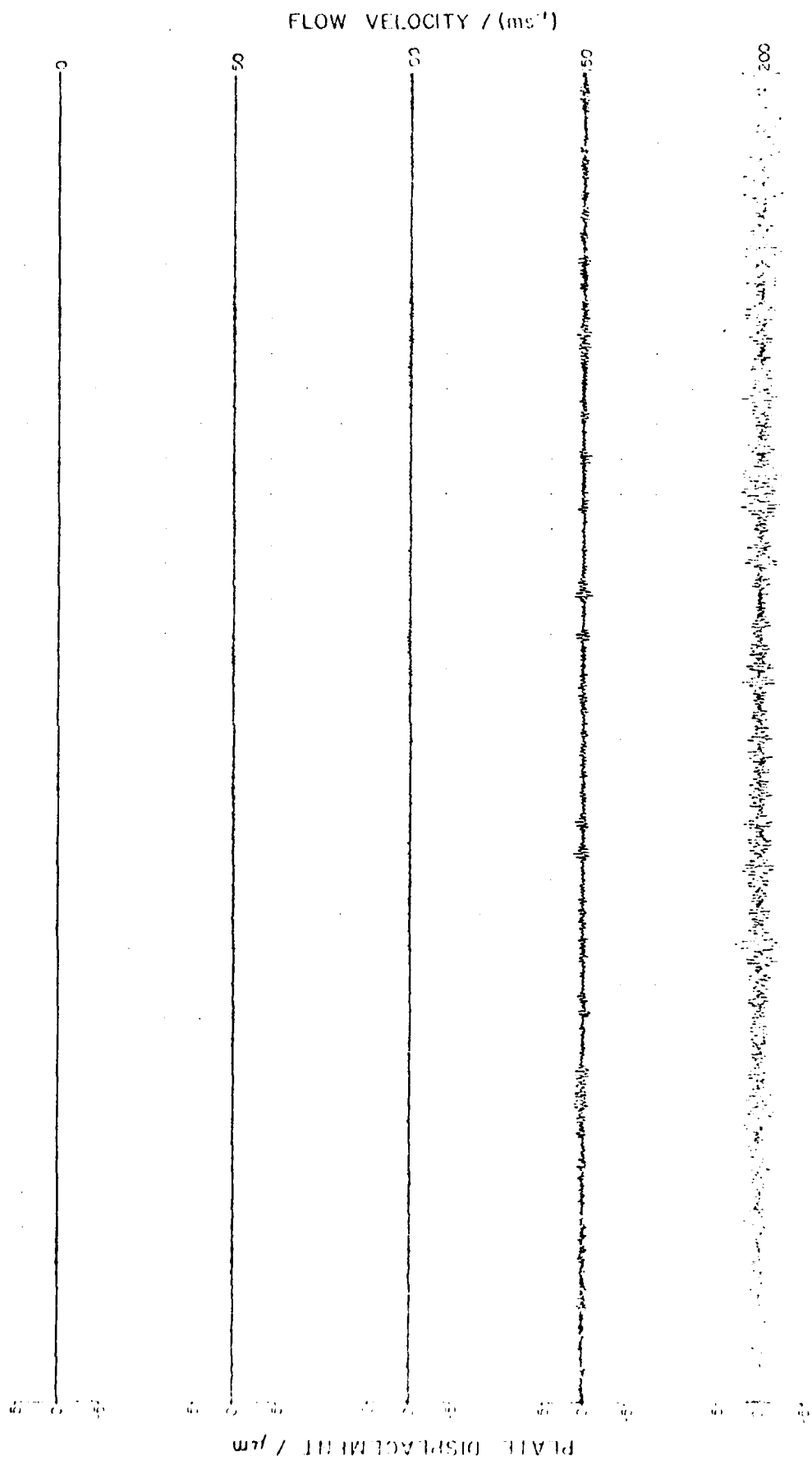


Figure 25

Performance Curves for the Automatic Control System
Under "Steady" Flow Conditions

PERFORMANCE OF DRAG BALANCE CONTROL SYSTEM



AD-A089 811

CAMBRIDGE UNIV (ENGLAND) CAVENTISH LAB
REDUCTION OF AERODYNAMIC DRAG.(U)
MAY 80 J CLARK, J E FIELD, W A WILBY

F/G 20/4

AFOSR-79-0057

UNCLASSIFIED

AFOSR-TR-80-0748

NL

2 OF 2

AD-A
C-11-80



END

DATE

FORMED

11-80

DTIC

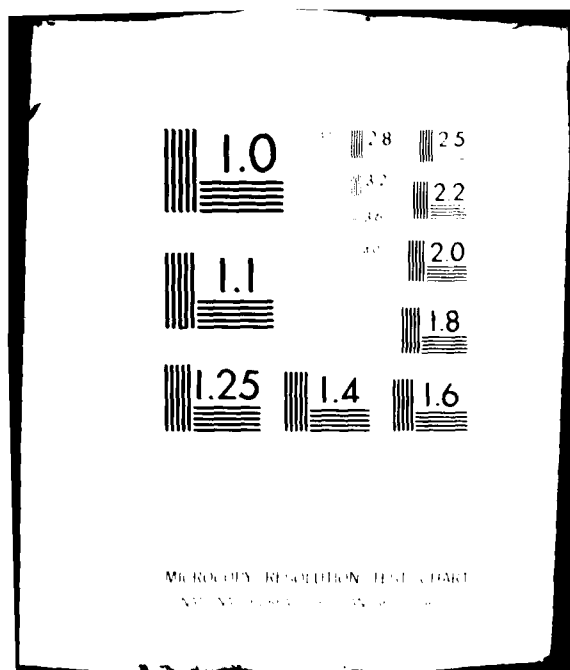
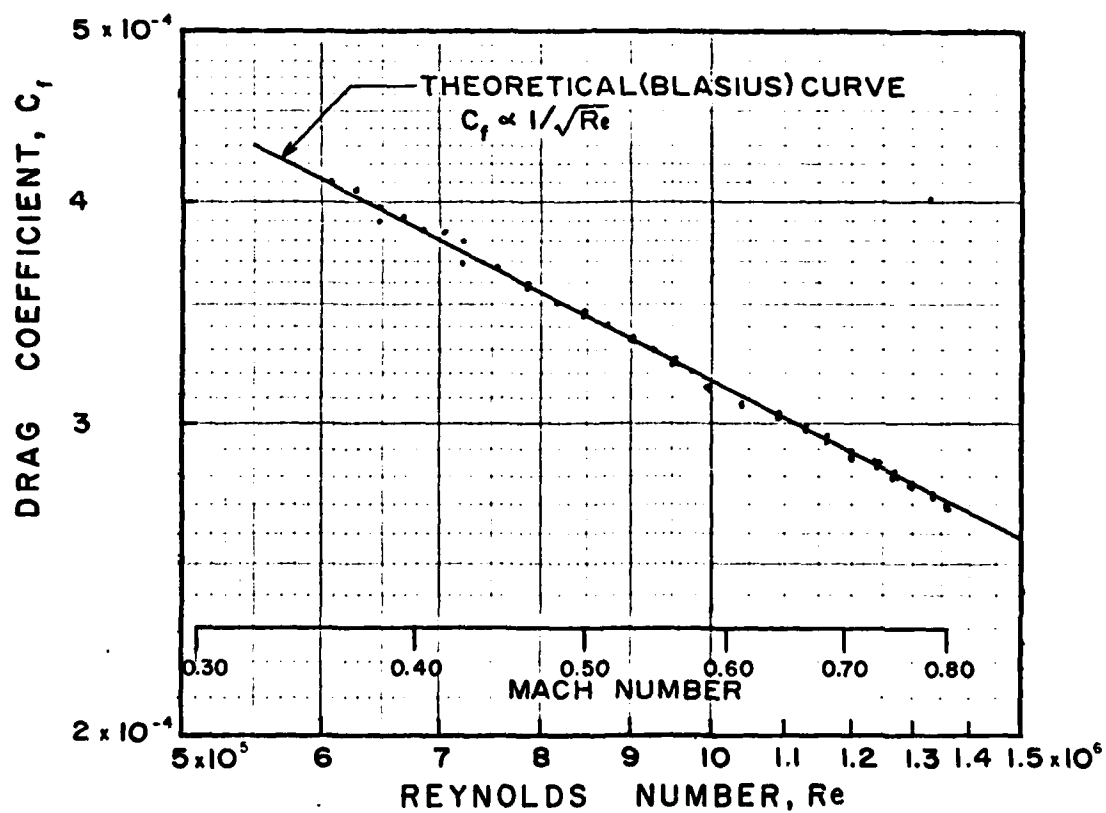


Figure 26

Drag Coefficient vs Reynolds Number

(Reynolds Number is based on
the plate length)



DRAG COEFFICIENT VS REYNOLDS NUMBER

Figure 27

Response Curve of Drag Balance

Amplitude Ratio vs Frequency of Forcing Function

DRAW BALANCE FREQUENCY RESPONSE CURVE

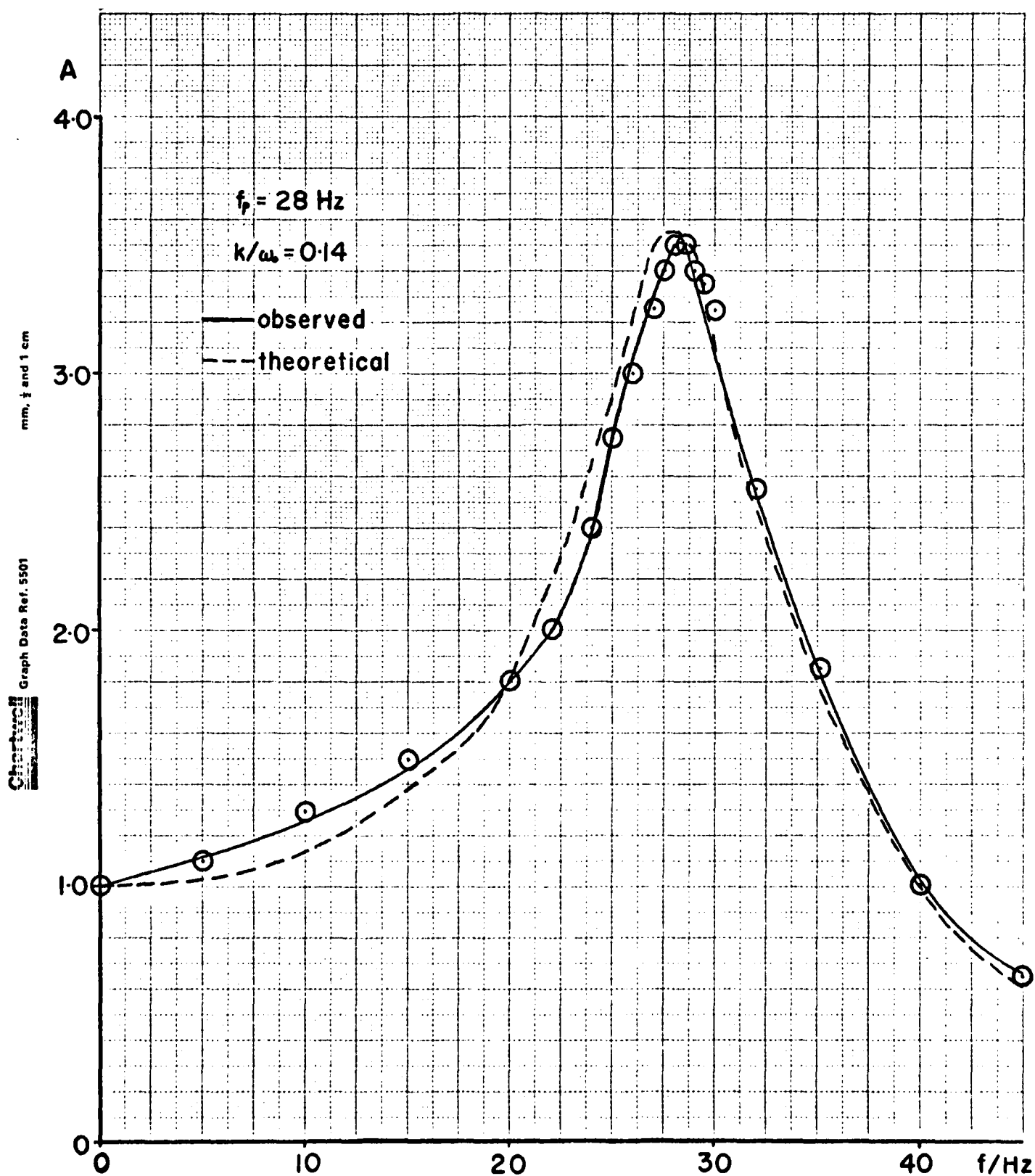


Figure 28

Initial Test of Drag Balance

Note that P_s /plate was measured with a mercury manometer,
 P_s on a precision dial manometer.

INITIAL TEST OF DRAG BALANCE

Log 4 Cycles x 3 Cycles

Graph Data Ref. 5943

WELL

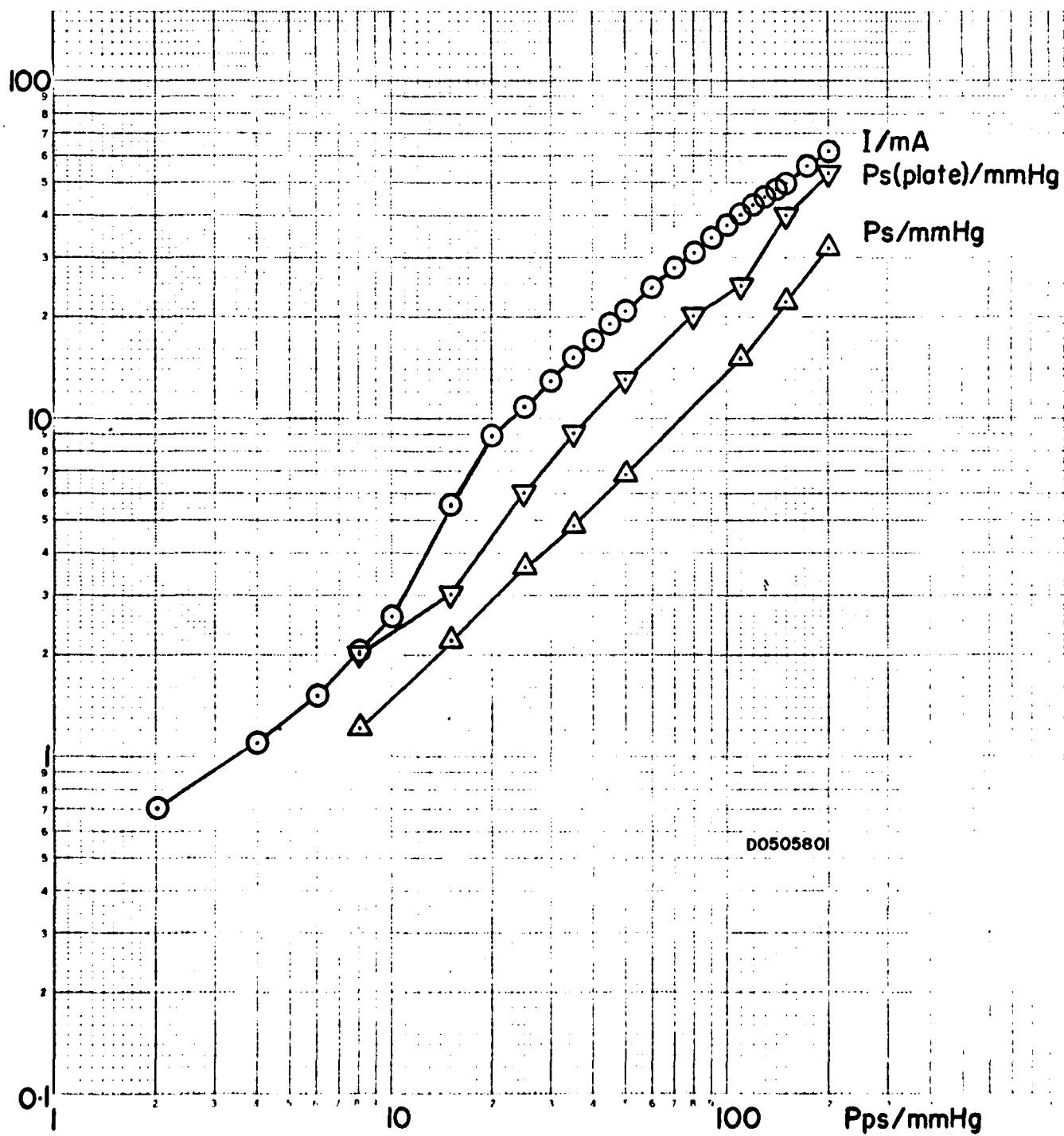


Figure 29

Coil Current vs Pitot Static Pressure

First Set of Test Data

COIL CURRENT vs PITOT STATIC PRESSURE

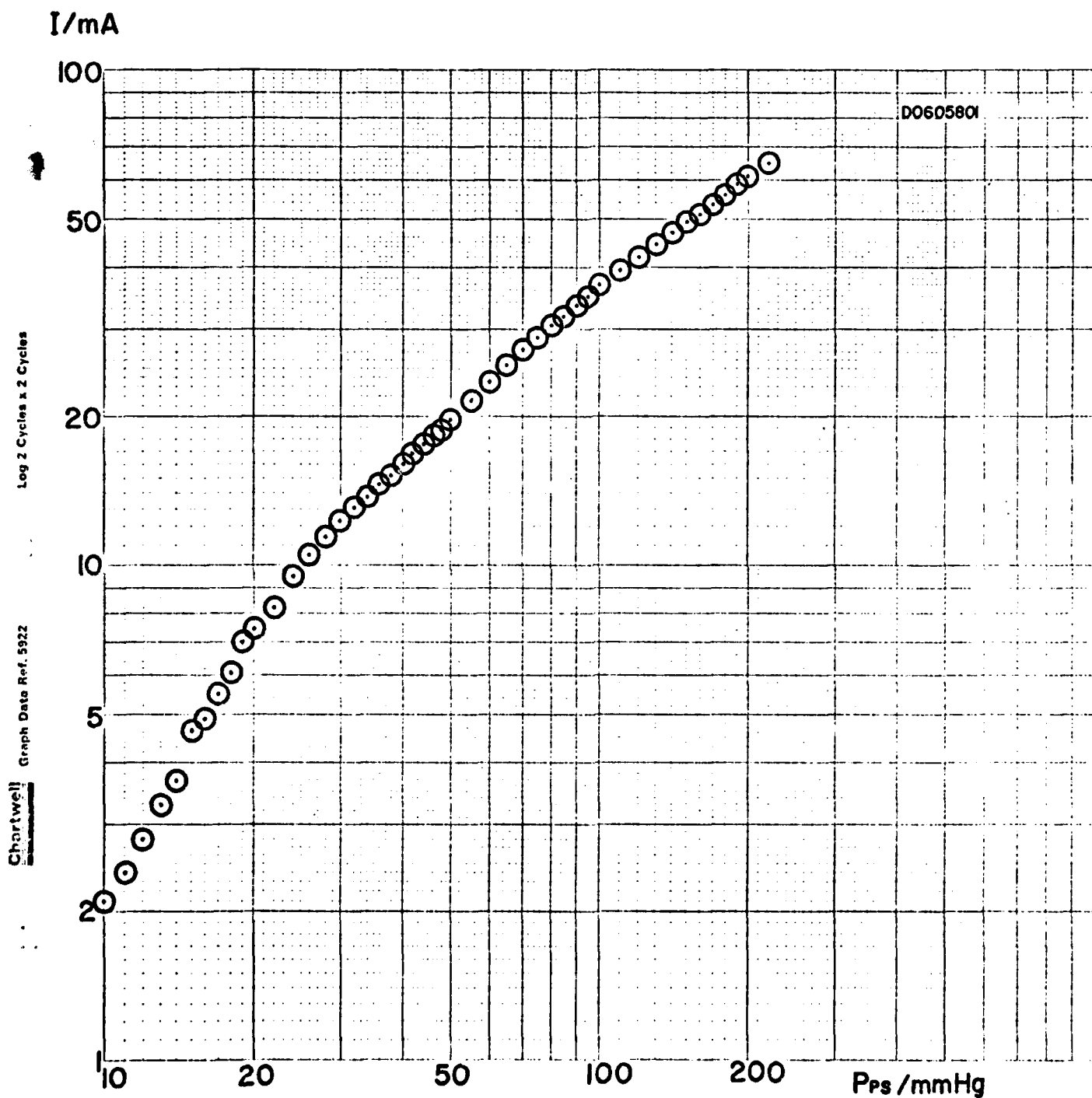


Figure 30

Typical Calibration Curve for the Drag Balance

Coil Current vs Load (number of bearings)

DRAG BALANCE CALIBRATION CURVE

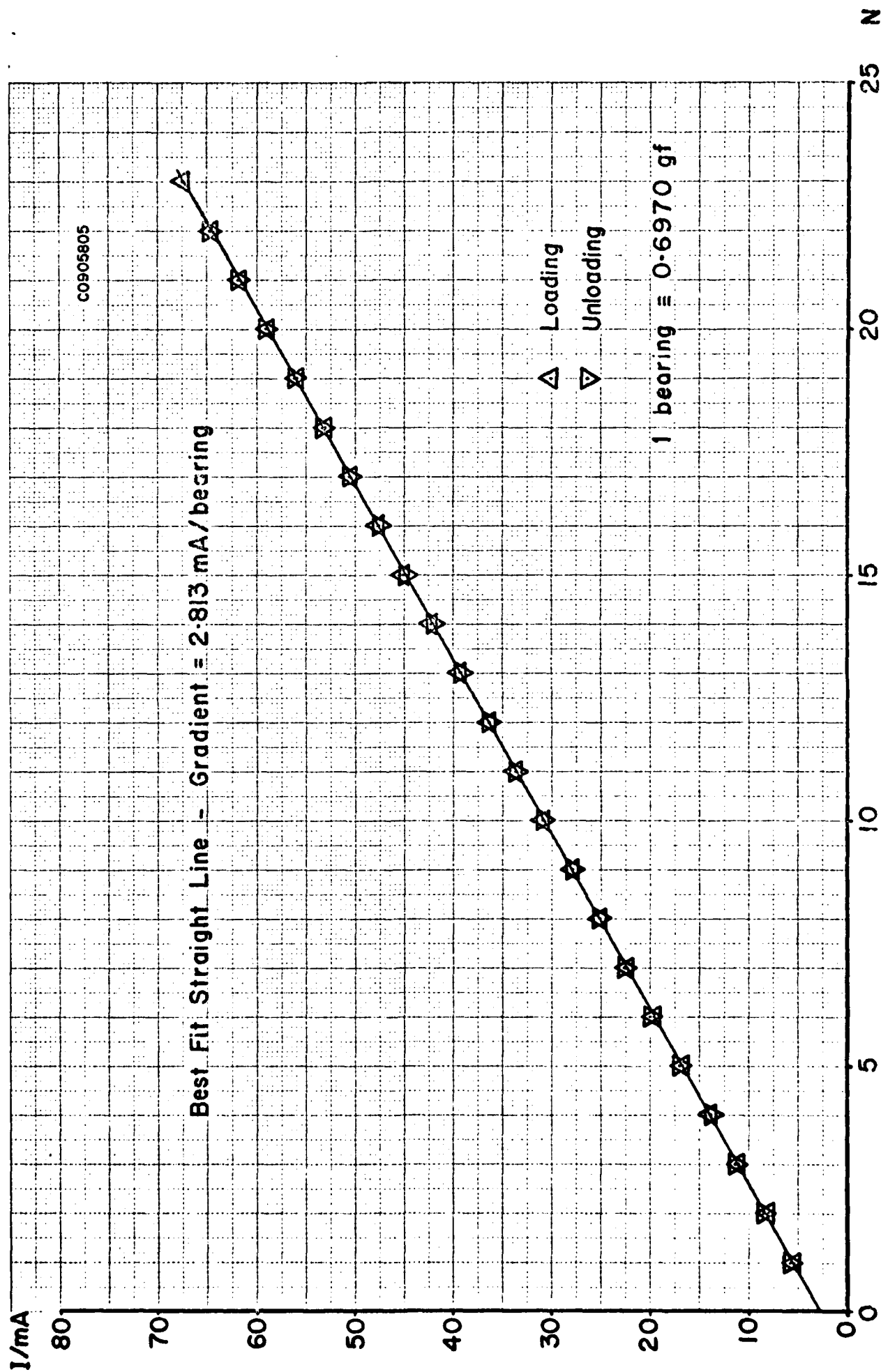


Figure 31

Drag Coefficient vs Reynolds Number

First Set of Test Data

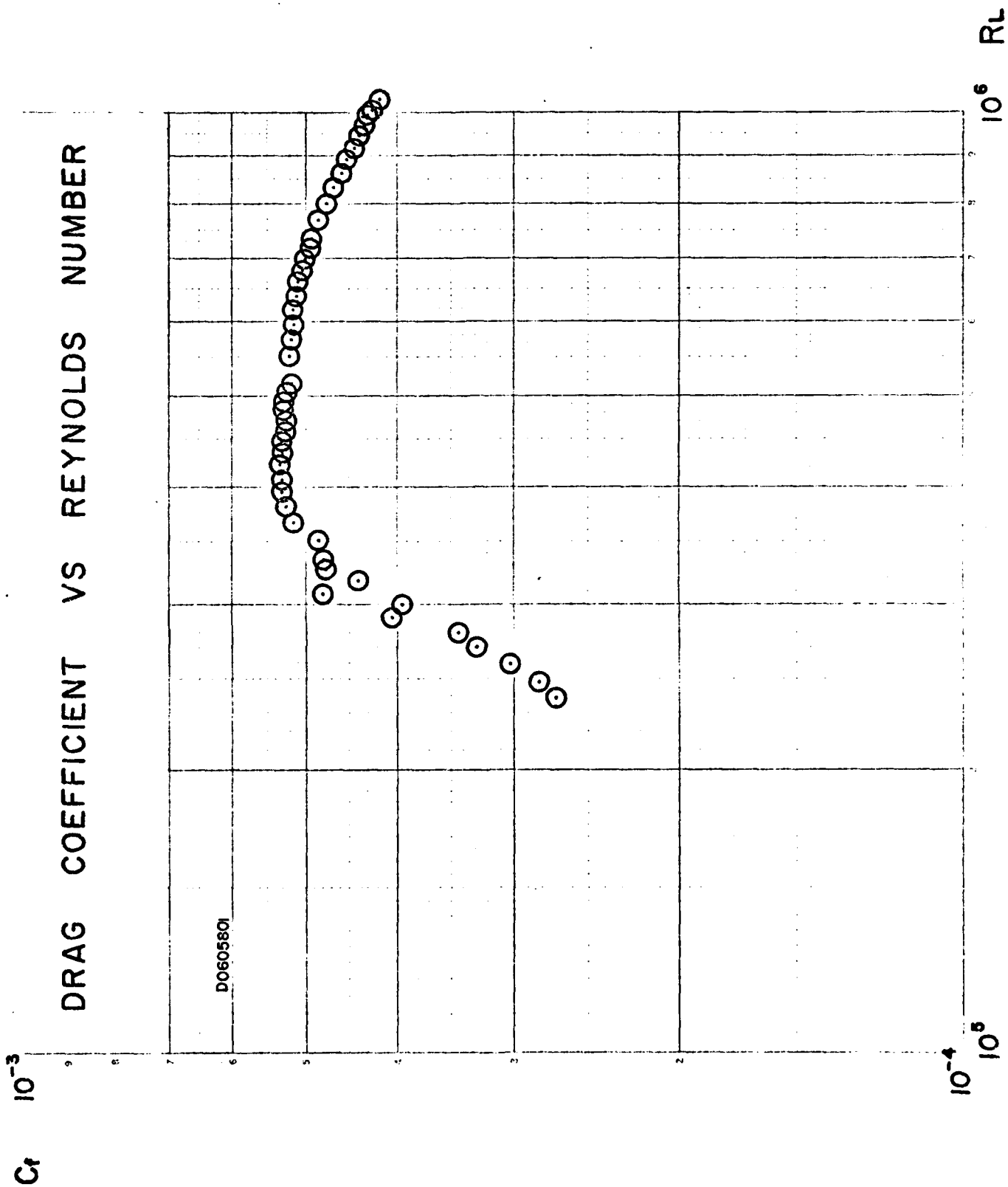


Figure 32

Coil Current vs Pitot Static Pressure

Second Set of Test Data

COIL CURRENT vs PITOTSTATIC PRESSURE

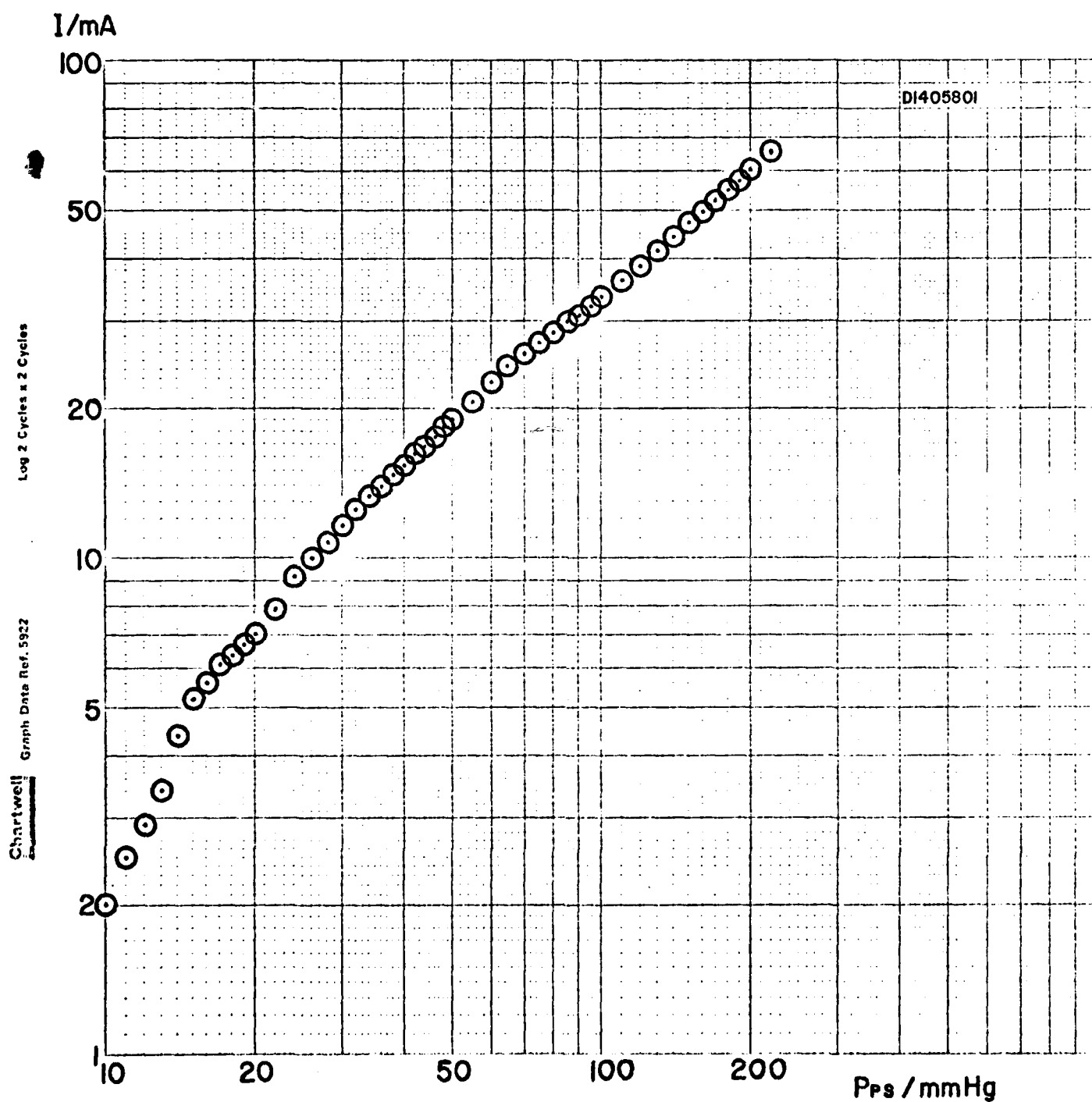


Figure 33

Diagram Showing the Foil Mounting Procedure

Note that the diagram is not to scale, and that the spring clips have been omitted for the sake of clarity.

RADIOACTIVE DRAG PLATE CONSTRUCTION

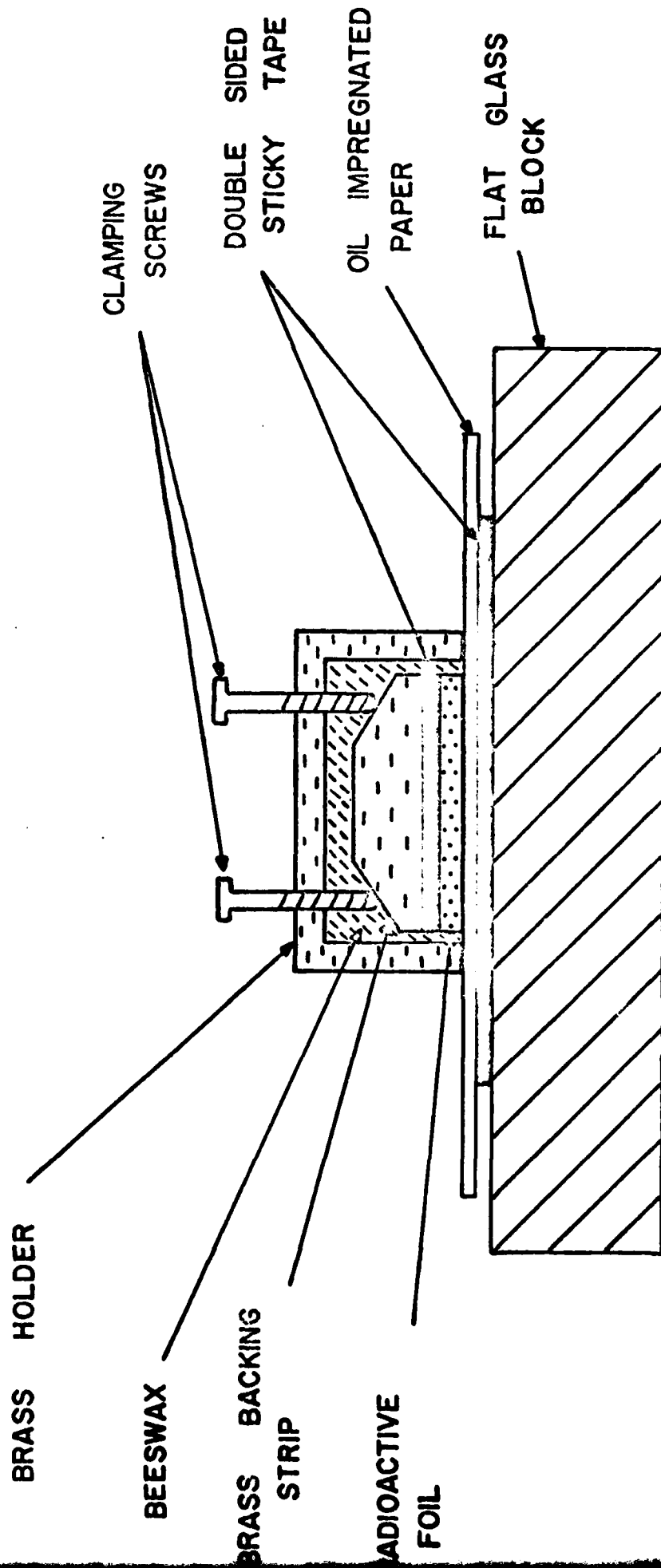


Figure 34

Photograph Illustrating the Precautions Taken When
Handling the Radioactive Sources

The shield which can be seen in the righthand side of the picture is constructed of 2" thick interlocking lead bricks. Behind the screen is a drag plate clamped as for mounting. In the left of the picture can be seen the radiation monitors used to check the degree of exposure to the sources, and to check for radioactive contamination.

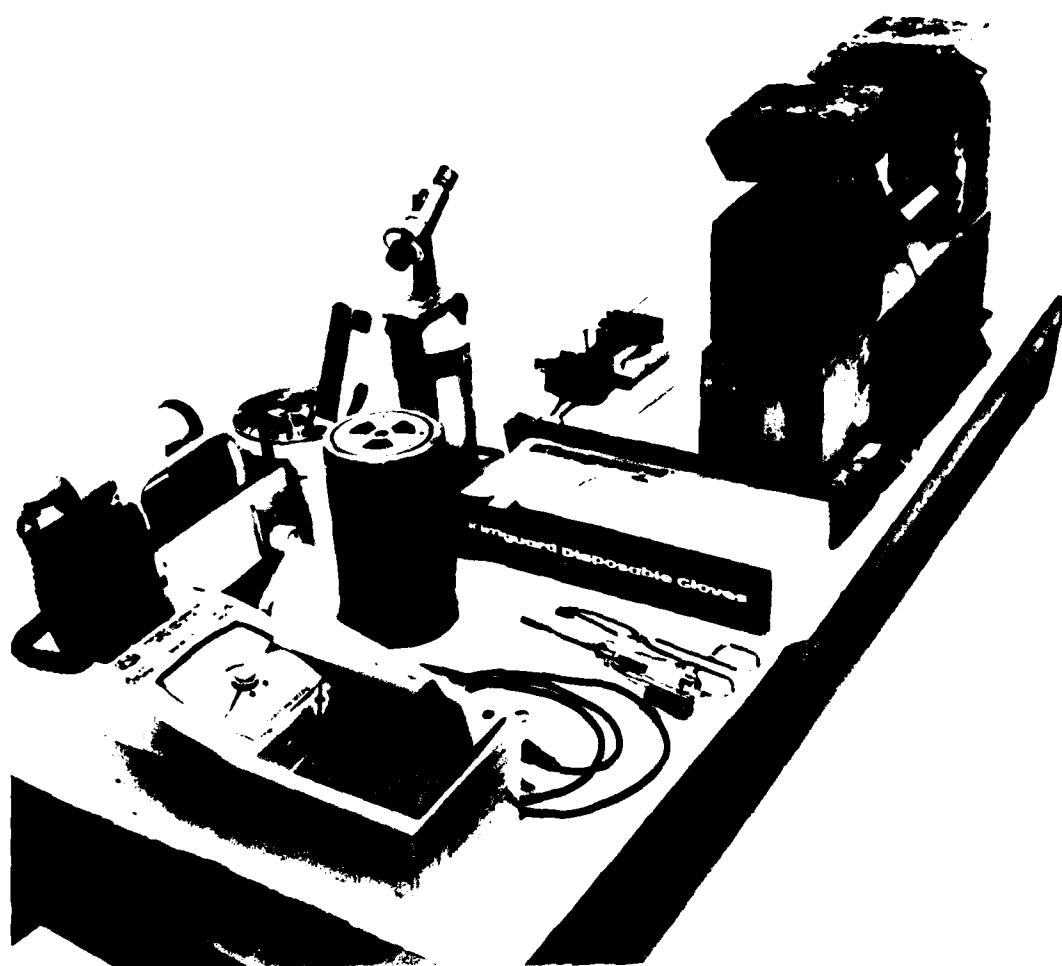
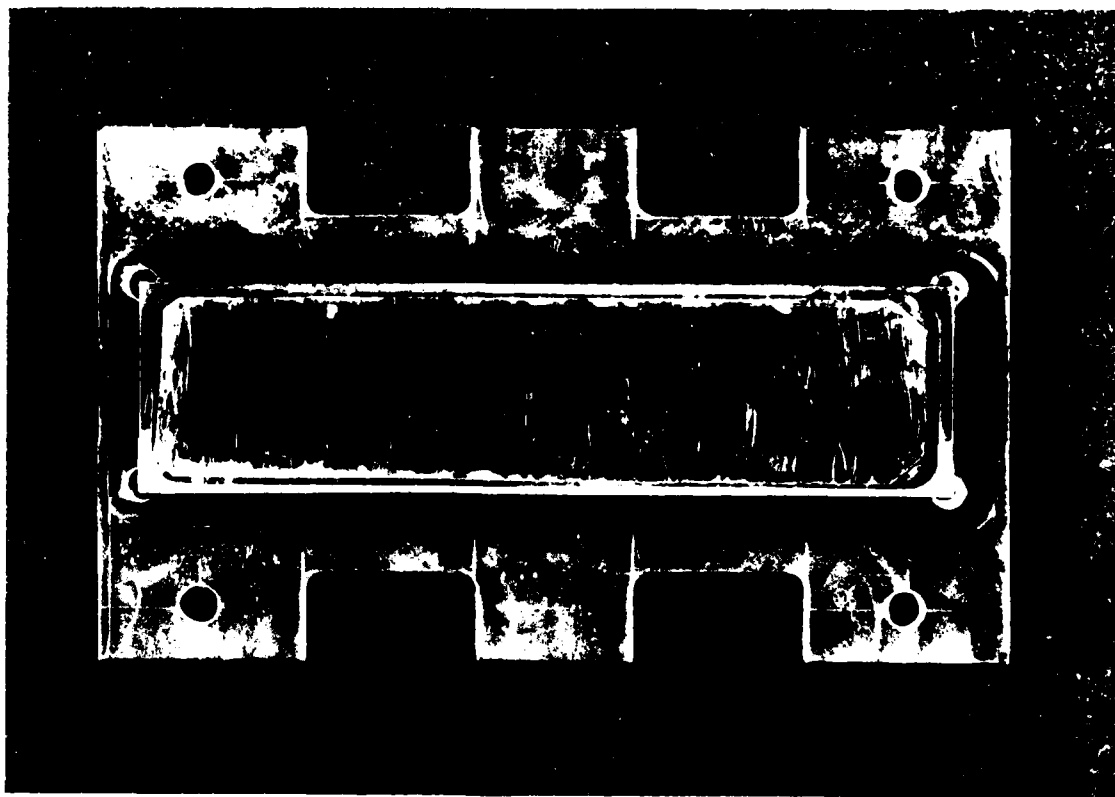


Figure 35

Active Drag Plate

This photograph shows a drag plate made up with a silver foil. The plate is fixed into a perspex holder by double sided sticky tape, ready for use in the experiment described in Section 3.6.

The surface scratches noticeable in the photograph are in fact very fine, but have been enhanced in the picture by the illumination used during the exposure.



4 Summary of Results

The drag balance can be readily calibrated to an accuracy approaching 0.1% and yields accurate drag measurements over the large part of the subsonic flow regime (~ 0.1 -0.8 Mach Number). Above ~ 0.35 Mach Number good agreement can be obtained with the Blasius Equation for the drag coefficient.

During operation the position of the drag plate is maintained to within $\sim 2 \mu\text{m}$ of the null position and the average position to considerably better than this.

Drag data taken for different plain drag plates shows reproducibility to a few percent.

In a preliminary experiment, skin friction drag reductions were observed on irradiating the flow over a plain brass plate with 0.2 MeV β particles from a 120 mCi ^{147}Pm source. The results are summarised below. Note that little importance should be attached to the two low flow measurements.

Flow Mach Number	% Drag Decrease
0.06	(40 \pm 20)
0.14	(15 \pm 15)
0.22	7 \pm 4
0.30	5 \pm 2
0.42	5 \pm 3
0.50	5 \pm 3
0.58	4 \pm 1

5 Discussion and Conclusions

The drag balance shows good accuracy and stability and the prospects of achieving a sensitivity of $\pm 0.5\%$ in drag measurements are excellent except at the lowest flow speeds where building vibrations are a problem.

The results obtained with β particle irradiation show that a decrease in drag force is taking place at atmospheric pressure. Variations in measurements due to differences in the foil mounting and plate positioning will be considered in more detail in future research; however, it is felt that the silver and promethium plates are sufficiently alike for the drag change observed to be taken as a real effect. Neglecting the very uncertain data at low velocities the results show a reduction in drag on irradiation of $\sim 5 \pm 3\%$. It is tempting to interpret the data as showing that the change in drag is smaller at higher flow speeds than lower. This would agree with our ideas on the mechanism of the effect (discussed below).

The changes in drag (or effective viscosity) are unlikely to be caused by the introduction of Coulomb forces due to ionisation in the air; the magnitude of this effect should be orders of magnitude smaller than that observed.

In both this work and that of Clark, Kestin and Shah, a conducting drag element was used; the interaction between the ions and image currents could act so as to reduce the viscous shear, but the magnitude of this effect is not known.

A conjecture is that the clustering of neutral species around the ions might be important; this obviously causes mobility changes, and it is possible that the clusters might also act in such a way as to inhibit the formation of turbulence at the molecular level. However, at present, there is insufficient knowledge about the density, structure

and stability of the clusters formed for any estimate to be made of the magnitude of this effect. Studies of the basic mechanisms involved in this phenomenon will form a major part of future research.

Appendix A Problems Encountered

The work was delayed earlier this year by the late arrival and inoperable condition of the air compressor. Both the Phillips PR9307 and the Schaevitz CAS-025 bridges broke down during the year, the repair of the latter being hindered by the unavailability of the correct circuit diagram. Except for these occasions the equipment has performed adequately.

It is probable that a different type of alpha foil will have to be used in future, as it is difficult to get a flat drag plate using the polonium foil.

Appendix B References

- | | | |
|---|--|---|
| 1 | Schlichting
McGraw-Hill, 1979 (7th ed.) | Boundary Layer Theory |
| 2 | Tritton
Van Nostrand-Reinhold, 1979 | Physical Fluid Dynamics |
| 3 | Goldstein
OUP, 1943 (2 vols) | Modern Developments in
Fluid Dynamics |
| 4 | Landau & Lifshitz
Pergamon, 1978 | Fluid Mechanics |
| 5 | Clark, J., Kestin, J. & Shah, V.L.
Physica <u>89A</u> (1977) pp 539-554 | Effect of Long Range Intermolecular
Forces on the Drag of an Oscillating
Disk and on the Viscosity of Gases |
| 6 | Kestin, J. & Shah, V.L.
AFFDL-TR-68-86 | as 5 |
| 7 | Dhawan, S.
NACA-1121 (1953) | Direct Measurements of Skin
Friction |
| 8 | Allen, J.M.
J. Fluid Engng., March 1977,
p 197 | Experimental Study of Error
Sources in Skin Friction Balance
Measurements |

Appendix C Bibliography

- | | |
|---|---|
| Bird, Stewart & Lightfoot
Wiley, 1960 | Transport Phenomena |
| Bradshaw
Pergamon, 1971 | An Introduction to Turbulence
and its Measurement |
| Curle & Davies
Van Nostrand-Reinhold, 1971 (2 vols) | Modern Fluid Dynamics |
| Daneshyar
Pergamon, 1976 | One-Dimensional Compressible
Flow |
| Douglas, Gasiorek & Swaffield
Pitman, 1979 | Fluid Mechanics |
| Hinze
McGraw-Hill, 1959 | Turbulence |
| Hirschfelder (ed.)
Wiley, 1967 | Intermolecular Forces (Adv. in
Chem. Phys, Vol. 12) |
| Hirschfelder, Curtiss & Bird
Wiley, 1954 | Molecular Theory of Gases &
Liquids |
| Kistenmacher, H., Lie, G.C.,
Popkie, H. & Clement, E.
J. Chem. Phys <u>61</u> (1974) pp 546-561 | Study of the Structure of
Molecular Complexes |
| McDaniel, Cermak, Dalgarno,
Ferguson & Friedman
Wiley, 1970 | Ion-Molecule Reactions |
| Margenau & Kestner
Pergamon, 1969 | Theory of Intermolecular
Forces |
| Massey
OUP, 1971 | Electronic & Ionic Impact
Phenomena |
| Monchick, L. & Mason, E.A.
J. Chem. Phys <u>35</u> (1961) pp 1676-
1697 | Transport Properties of
Polar Gases |
| Mueller, C.R. & Brackett, J.W.
J. Chem. Phys <u>40</u> (1966) pp 654-661 | Quantum Calculations of the
Sensitivity of Diffusion,
Viscosity and Scattering Experiments
to the Intermolecular Potential |
| Plint & Böswirth
Charles Griffin & Co., 1978 | Fluid Mechanics |
| Townsend
CUP, 1976 (2nd ed.) | The Structure of Turbulent
Shear Flow |

- | | |
|---|---|
| Kistenmacher, H., Lie, G.C.,
Popkie, H. & Clement, E.
J. Chem. Phys <u>61</u> (1974) pp 546-561 | Study of the Structure of
Molecular Complexes |
| Landau & Lifshitz
Pergamon, 1978 | Fluid Mechanics |
| Ling, S.C. & Liang, T.Y.
J. Fluid Mech. <u>65</u> (1974) pp 499-
512 | Anomalous Drag Reducing
Phenomenon at a Water/Fish
Mucus or Polymer Interface |
| McDaniel, Cermak, Dalgarno,
Ferguson & Friedman
Wiley, 1970 | Ion-Molecule Reactions |
| Margenau & Kestner
Pergamon, 1969 | Theory of Intermolecular
Forces |
| Massey
OUP, 1971 | Electronic & Ionic Impact
Phenomena |
| Monchick, L. & Mason, E.A.
J. Chem. Phys <u>35</u> (1961) pp 1676-
1697 | Transport Properties of
Polar Gases |
| Mueller, C.R. & Brackett, J.W.
J. Chem. Phys <u>40</u> (1966) pp 654-
661 | Quantum Calculations of the
Sensitivity of Diffusion,
Viscosity and Scattering Experiments
to the Intermolecular Potential |
| Plint & Böswirth
Charles Griffin & Co., 1978 | Fluid Mechanics |
| Reshotko, E.
J. Aircraft <u>16</u> (1979) pp 584-590 | Drag Reduction by Cooling in
Hydrogen Fueled Aircraft |
| Schlichting
McGraw-Hill, 1979 (7th ed.) | Boundary Layer Theory |
| Daneshyar
Pergamon, 1976 | One-Dimensional Compressible Flow |
| Townsend
CUP, 1976 (2nd ed.) | The Structure of Turbulent
Shear Flow |
| Tritton
Van Nostrand-Reinhold, 1979 | Physical Fluid Dynamics |
| Wells (ed.)
Plenum, 1969 | Viscous Drag Reduction |